

Numerical derivation of a normal contact law for compressible plastic particles

B. D. Edmans^{a,*}, I. C. Sinka^a

^a*University of Leicester, University Road, Leicester LE1 7RH, United Kingdom*

Abstract

A new contact law is proposed to describe the behaviour of plastically compressible particles. The law was derived from contact simulations in which a general continuum constitutive model, the von Mises Double Cap (VMDC) model, was introduced to represent the particle material behaviour, allowing distinct dilatatory, shearing and densification plastic flow regimes. Elastic and plastic properties were prescribed as functions of density. Parametric studies were conducted covering the parameter space of published experimental data for a range of pharmaceutical powders and granules.

The analysis showed plastic zones corresponding to the three flow regimes developing within the particle, with size, shape, location and onset conditions being dependent on the strength ratios of the constitutive model. The contact law established combines an initial quasi-linear region followed by an exponential hardening region, arising from the initiation, growth and hardening of plastic zones, and the development of dense and stable load-bearing structures.

The outcome of these studies is a new contact law, relationships for predicting contact law parameters from material parameters for both loading and unloading, and guidelines for the analytical treatment of plastic compressibility in particle contact. The contact law can be employed in discrete element and homogenisation models to predict macroscopic properties of porous granular materials, while the analytical framework and qualitative findings can be used in the design of granules.

Keywords: Contact law, Compressible plasticity, Constitutive model, Granule deformation, Finite elements

1. Introduction

1 Considerable efforts have been made in recent decades to increase understanding and predictability of the
2 behaviour of granular materials using models which represent the spatial arrangement of their constituent
3 particles explicitly and compute their interactions. Popular approaches for simulating the bulk mechanical
4 behaviour of granular media, including the discrete element method (DEM) (Cundall and Strack, 1979)
5 micromechanical models (Fleck et al., 1992) and homogenisation approaches (Chang and Gao, 1995), make
6 use of contact laws which describe the relationship between the relative displacement of particle centres and
7 contact force resultants for two spheres in contact.

8 The problem of determining normal force-displacement relations describing solid spherical bodies in
9 contact is of considerable heritage and there exists an extensive literature concerned with their development.
10 Pioneering work was carried out by Hertz (1882), who derived a closed-form relation for elastic spheres in
11 point contact. Relations describing elastic, plastic and combined behaviour have been formulated by Kogut
12 and Etsion (2002), Jackson and Green (2005), among others. Modifications for elastoplastic materials
13 including hardening have been described by Shankar and Mayuram (2008) and others. A review of contact
14 relations for elastoplastic particles is provided by Ghaednia et al. (2018).

*Corresponding author. Email: bde2@leicester.ac.uk

15 However, in the development of elastoplastic contact laws it is assumed that the sphere material exhibits
16 classical (von Mises) plastic behaviour, where plastic deformation takes place at constant volume. Thus,
17 to date, contact laws which capture the densification behaviour of compressible particles have not yet been
18 formulated. The behaviour of compressible particles is of practical interest for many applications. Typically,
19 such particles result from agglomeration processes and contain internal voids which may change in size or
20 shape, redistribute, coalesce, or close when loading is applied to the particle. The importance of the influence
21 of particle internal void fraction on the final deformation state attained by a particles assembly has been
22 shown by [Johansson et al. \(1995\)](#), who carried out investigations using instrumented die compaction of
23 powders. Consequently, as a preliminary to proposing models for particle materials, a short survey of
24 constitutive models for compressible plasticity is warranted.

25 The behaviour of granular materials in bulk is commonly described using continuum compressible elasto-
26 plasticity models. In the field of soil mechanics, models such as the critical state (Cam-Clay) models ([Roscoe
27 et al., 1958](#)), Drucker-Prager Cap model ([Drucker and Prager, 1952](#)), and Mohr-Coulomb model ([Coulomb,
28 1776](#); [Mohr, 1900](#)) have gained widespread acceptance in engineering practice and have been adapted for
29 other applications, including the modelling of metal powder compaction (see, for example, [Trasorras et al.
30 \(1989\)](#)). These models define a set of stresses from which deformations will be fully recoverable on unloading
31 (specified by the yield function), a functional (the flow potential function) prescribing the plastic flow that
32 may occur when the stress state reaches the boundary of this set, and rules describing how this set changes
33 based on the loading history. Typically, isosurfaces of the yield function are prescribed to expand uniformly
34 in stress space with increasing volumetric plastic strain (isotropic hardening), but translations of the yield
35 surface in stress space with deviatoric plastic strain may also be considered (see, for example, [de Boer and
36 Brauns \(1990\)](#)). Even greater flexibility in the definition of appropriate plasticity models can be achieved
37 by calibrating generalized plasticity or hypoplastic models. As it is not always practical to conduct triaxial
38 tests to determine the Lode angle dependence of plasticity models, it is common to define both elastic and
39 plastic components in terms of scalar volumetric and deviatoric measures of stress (related to invariants I_1
40 of the stress tensor and J_2 of the deviatoric stress tensor) and corresponding strain measures.

41 It is common to combine compressible plasticity models with elastic models employing moduli dependent
42 on the compression state. Hyperelastic models in which elastic stresses are obtained from a potential function
43 representing stored elastic energy have been developed for granular materials (see, for example, [Szanto
44 et al. \(2008\)](#)), which ensure thermodynamic admissibility of the constitutive model. However, in practical
45 investigations it is not always possible to determine a unique set of hyperelastic parameters which adequately
46 reproduce the material response over the loading range, and often a hypoelastic description is preferred, in
47 which elastic moduli are defined for different values of relative density. Relative density is defined as the
48 ratio of current (apparent) density to the maximum density attainable by compaction. This is closely related
49 to volumetric plastic strain, that is, state variables defined in the plastic part of the model. Relative density
50 is often chosen as the only state variable for reasons of simplicity and practical utility; it is straightforward
51 to measure and often used in the product specification. Alternatively, [Borja \(1991\)](#) describes algorithms
52 for implementing models where elastic moduli are dependent on volumetric elastic strain. However, it
53 appears reasonable to suppose that the elastic or unloading response of a granular compact is in some
54 way dependent on its consolidation state, characterised by its volumetric plastic strain ([Houlsby, 1981](#)) or
55 stress state ([Duncan and Chang, 1970](#)). A popular approach among investigators modelling bulk powder
56 compaction for including dependence on plastic strain is described by [Cunningham et al. \(2004\)](#); [Sinka et al.
57 \(2003\)](#) and others, where variation of the total (not incremental) elastic modulus with relative density is
58 prescribed and an explicit scheme is used to update the elastic parameters. An alternative, fully implicit
59 implementation that improves accuracy and computational efficiency is presented by [Edmans and Sinka
60 \(2019\)](#).

61 Particles of importance in engineering display a wide variation in mechanical and physical properties. A
62 general summary of the mechanical properties of agglomerated particles is provided by [Bika et al. \(2001\)](#) and
63 a study of their structure is detailed by [Barrera-Medrano et al. \(2007\)](#). The degree of porosity (quantified
64 as one minus relative density) exhibited by agglomerated particles used in pharmaceutical applications
65 is comparable in magnitude to interparticle void fractions ([Macias and Carvajal, 2012](#)), supporting the
66 argument that particle compressibility should be considered in particle interaction models.

67 The evolution of elastic parameters due to densification has received attention from a number of authors.
68 [Walton \(1987\)](#) developed an analytical model assuming a random packing of uniform elastic spheres and
69 the Hertz contact law, which was used to calculate effective elastic moduli of assemblies of spheres. The
70 model predicts that the stiffness of an assembly increases with the product of power-law functions of relative
71 density, average number of contacts and applied pressure. [Duckworth \(1953\)](#) proposed that Young’s Modulus
72 of porous materials should be an exponential function of relative density. The porous elasticity model,
73 implemented in the finite element (FE) analysis code Abaqus ([Dassault Systèmes, 2014](#)), uses a quasi-
74 exponential dependence of the elastic bulk modulus on volumetric elastic strain.

75 Realistic models for the evolution of yield strength should predict that plastic compressibility and
76 pressure-sensitivity of yield surfaces vanishes as porosity approached zero, as the material loses the capability
77 to deform by reducing void fraction. This implies that hydrostatic yield pressure approaches infinity asymp-
78 totically and yield strength in shear approaches a constant, finite value. Several rules have been proposed to
79 model the transition between pressure-sensitive and pressure-independent plasticity, most notably the modi-
80 fied Gurson model ([Tvergaard, 1990](#)), which incorporates a natural limit to hardening such that the material
81 bulk yield behaviour approaches that predicted by the von Mises model as full density is approached. Nev-
82 ertheless, approximating the dependence of yield strength as an exponential function of relative density has
83 been found to be adequate if full density is not approached too closely, as in the following examples. The
84 hardening rule for the original Cam-Clay model ([Roscoe et al., 1958](#)) prescribes an exponential increase in
85 yield strength with relative density. [Macias and Carvajal \(2012\)](#) found an exponential relationship between
86 the strength of granules and their density. [Maeda and Miura \(1999\)](#) find that an exponential model is also
87 suitable for noncohesive granular materials, such as sand, while [Spriggs \(1961\)](#) found it suitable for porous
88 ceramic materials. Die compaction experiments (for example, [Cunningham et al. \(2017\)](#)) have also found
89 exponential relationships to be appropriate for describing pharmaceutical excipient powders in bulk.

90 In spite of a vast literature concerning contact laws, and the existence of constitutive laws for compressible
91 materials, to the authors’ knowledge contact laws for compressible particles have not yet been developed.
92 Contact laws for compressible particles are important because in many cases, the porosity of a particle is
93 significant in magnitude and influences the load-displacement response appreciably, as demonstrated later
94 in this paper. It is proposed that incorporating particle compressibility effects in larger-scale models via
95 improved contact laws will increase understanding and predictability of industrial processes. The approach
96 and findings of the current work may be compared to other studies investigating the influence of material
97 parameters on the load-displacement response of spheres in contact. These include [Alcalá and Esqué-
98 los Ojos \(2010\)](#), who used finite elements to investigate elastoplastic materials with von Mises plasticity
99 and power-law hardening, and [Russell and Wood \(2009\)](#), who used analytical methods to investigate the
100 influence of the tensile to compressive strength ratio in a damage-plasticity model.

101 The article is organised as follows: in Section 2, a new constitutive model including hardening plas-
102 ticity and elastic moduli which vary with volumetric plastic strain is introduced as a candidate model for
103 compressible particles. In Section 3, a set of general material parameters for describing compressible plas-
104 tic models is defined. Published data from die compaction testing are used to determine a representative
105 base case and envelope of typical values of material parameters for pharmaceutical excipients, for use in
106 subsequent parametric studies. Parametric finite element studies are described in Section 4 which establish
107 load-displacement response for particles with a range of material properties. Results are presented in Sec-
108 tion 5, including both load-displacement response and development of plastic zones. Results are presented
109 for different plasticity models, and for combinations of parameters representing extreme ends of the chosen
110 simulation space. A novel contact law for compressible particles is presented in Section 6 based on a com-
111 prehensive set of simulations using the new constitutive model. The results of a secondary fitting procedure
112 establishing a relationship between material parameters and contact law parameters is shown. Results are
113 presented for both loading and unloading, giving expressions suitable for implementation in DEM software.
114 Discussion and conclusions are presented in Sections 7 and 8, respectively.

115 In this article, “compressible particle” is used to refer to a particle that is made of a material that can
116 undergo densification, such as a porous granule. “Particle material” refers to a homogenised representation
117 of the particle’s constituents or Lagrangian continuum mechanics model that simulates its behaviour. “Sub-
118 particle” denotes any identifiable region within a particle’s volume showing greater continuity in displacement

119 field than the particle as a whole.

120 2. Von Mises Double Cap (VMDC) model for compressible material behaviour

121 Compressible particles present features similar to those of porous rocks/soils or powder materials un-
122 dergoing compaction: 1) their mechanical response is sensitive to pressure, leading to different strengths in
123 tension and compression, tensile strength being relatively low; 2) they can exhibit large inelastic deforma-
124 tions which involve significant volumetric plastic strain, leading to reduction of porosity (densification) and
125 3) both elastic and plastic properties evolve as the material densifies. Therefore constitutive laws capable of
126 reproducing such behaviour will be considered for the development of a contact law for compressible parti-
127 cles. In the following development, it will be assumed that deformation fields within compressible particles
128 can be considered continuous at all times. Consequently, this approach is most appropriate for representing
129 particles in which the characteristic internal pore size is small in relation to the particle diameter.

130 As starting point for investigation, the Drucker-Prager Cap (DPC) model is considered, using the implicit
131 assumption that the constitutive behaviour for the particle is equivalent to that of a compacted powder.
132 The yield surface of the DPC model (shown in Fig. 1) is composed of a shear failure line and compaction
133 cap. These features allow two key phenomena observed in granular media: the increase in density that can
134 occur due to plastic flow when the stress state of the material is on the curved compaction segment of the
135 yield surface, and the dilatatory plastic flow which can occur when the stress state is on the shear failure
136 line, respectively. The latter feature also represents the increasing resistance to deviatoric loading that is
137 manifest when hydrostatic pressure increases.

138 However, when considering models for materials, for compressible particles, there is a need to strengthen
139 the shear failure line. The bonding between sub-particles, of whatever nature, may be stronger in resistance
140 to shear, and their shear strength may have less dependence on the normal force than implied by the DPC
141 model. This consideration led the authors to propose the von Mises Double Cap yield surface for compressible
142 particle materials. The yield surface for the VMDC model is shown in Fig. 1. The proposed constitutive
143 model has four key features. Firstly, the model is intended to compute the evolution of ductile, compressible
144 materials during plastic yield by integrating a plastic flow rule; it is not intended to describe the current
145 set of limit states only. Secondly, the formulation does not introduce indirect dependence of the material's
146 resistance to deviatoric loading on the degree of hydrostatic compaction experienced by the material (as in the
147 DPC model); instead, shear strengthening behaviour may be reproduced by defining appropriate hardening
148 laws explicitly. Relatedly, the fact that the size and shape of the tensile cap region of the yield surface
149 are controlled by parameters that are independent of the degree of compaction allows greater flexibility in
150 representing admissible stress states and plastic flow behaviour when hydrostatic stress is tensile. Finally,
151 algebraic expressions for the yield function, flow rule and their associated partial derivatives are simpler
152 than those used required by the DPC model, implying less risk of transcription errors on implementation.
153 Thus, the VMDC model is one of the simplest possible yield surfaces that can describe compressible plastic
154 behaviour and is capable of sustaining significant shear loads.

155 In this Section, the yield functions, flow potential functions, hardening laws, and evolution laws relating
156 yield function parameters to state variables are detailed for the VMDC and DPC models. For comparison,
157 the von Mises (VM) model is included, which is later used both in perfectly plastic form (VM-PP), and
158 with isotropic hardening. Generalised yield function parameters are employed to characterise plasticity
159 models. Hydrostatic yield pressure is denoted with σ_y , maximum shear strength with Γ and maximum
160 tensile strength with Λ . The axis ratio of the elliptical compaction section of the yield surface (where it
161 exists) is denoted with ϵ . Corresponding initial values are denoted with σ_{y0} , Γ_0 , Λ_0 and ϵ_0 , respectively.
162 Model-specific yield function parameters are denoted by π_i . Model components are expressed in terms of
163 the hydrostatic stress p and equivalent stress q . Yield surfaces for the plasticity models considered in p-q
164 space are shown in Fig. 1, where equal values of the shared yield function parameter $\pi_4 = \sigma_y$ are used to
165 form equivalent surfaces. Expressions for the yield and flow potential functions used in this work are listed
166 in Table 2. A summary of all symbols used in this article is provided in Table 1.

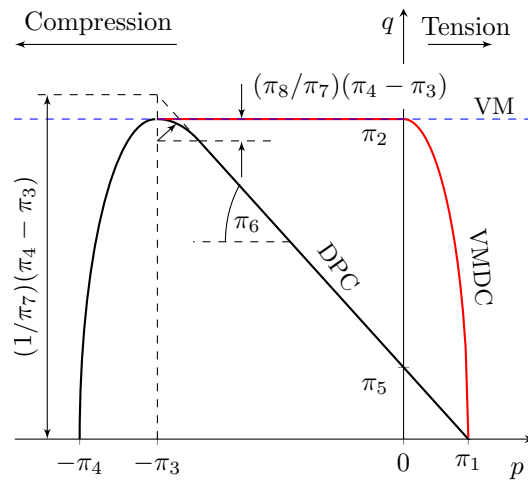


Fig. 1. Three yield surfaces in p - q space: von Mises (VM), Drucker-Prager Cap (DPC) and von Mises Double-Cap (VMDC)

Table 1 Nomenclature

Abbreviation*	Meaning
a	Hardening exponent (contact law parameter) [-]
\mathbf{D}_p	Plastic rate of deformation tensor [s^{-1}]
d_v^p	Rate of volumetric plastic deformation [s^{-1}]
E	Young's Modulus [Pa]
\bar{E}	Dimensionless stiffness
e_a	Area error [-]
e_p	Peak error [-]
F	Normal contact force [N]
\bar{F}	Dimensionless normal contact force
k	Initial stiffness (contact law parameters) [-]
k_{H0}	Dimensionless contact stiffness (Hertz law)
p	Hydrostatic stress [Pa]
q	Equivalent stress [Pa]
R	Particle radius [m]
VM(-PP)	Von Mises (- Perfectly Plastic)
DPC	Drucker-Prager Cap
VMDC	Von Mises Double-Cap
α	Particle unloading exponent [-]
β	Particle secant unloading stiffness [-]
Γ	Shear strength [Pa]
$\bar{\Gamma}$	Ratio of shear to compressive yield strength [-]
$\bar{\delta}$	Dimensionless normal particle displacement
$\bar{\delta}_t$	Transition displacement (dimensionless) between linear
$\bar{\delta}_{H0}$	Separation displacement (dimensionless) during unloading
ϵ	Eccentricity of compaction ellipse in yield surface [-]
ε	Strain [-]
ζ	Shear yield strength hardening exponent [-]
η	Hydrostatic yield strength hardening exponent [-]
Λ	Tensile strength [Pa]
$\bar{\Lambda}$	Ratio of tensile to compressive yield strength [-]
ν	Poisson's Ratio [-]
ξ	Stiffness increase exponent [-]
ξ_1	Poisson's ratio increase factor [-]
ξ_2	Compression cap eccentricity increase factor [-]
π_i	Yield surface parameters
ρ_r	Relative density [-]
σ_y	Yield strength in hydrostatic compression [Pa]
ϕ	State variable
ω	Tensile yield strength hardening exponent [-]

*zero subscripts indicate initial values of parameters,
superimposed dots indicate pseudotime derivatives

Table 2Yield functions (f) and flow potential functions (g) for the models investigated.

Name	Yield function/Flow potential function
von Mises (VM)	$f(p, q, \boldsymbol{\pi}) = g(p, q, \boldsymbol{\pi}) = \left(\frac{q}{\pi_2}\right)^2 - 1$
von Mises Double Cap (VMDC)	$f(p, q, \boldsymbol{\pi}) = g(p, q, \boldsymbol{\pi}) = \begin{cases} \left(\frac{p}{\pi_1}\right)^2 + \left(\frac{q}{\pi_2}\right)^2 - 1, & p > 0 \\ \left(\frac{q}{\pi_2}\right)^2 - 1, & 0 \geq p \geq -\pi_3 \\ \left(\frac{p+\pi_3}{\pi_4-\pi_3}\right)^2 + \left(\frac{q}{\pi_2}\right)^2 - 1, & p < -\pi_3 \end{cases}$
Drucker-Prager Cap (DPC)	$f(p, q, \boldsymbol{\pi}) = \begin{cases} q + p \tan \pi_6 - \pi_5 & p > -p_i \\ \sqrt{(p + \pi_3)^2 + (q - (1 - A)C)^2} - \pi_8 C & -p_i \geq p \geq -\pi_3 \\ \sqrt{(p + \pi_3)^2 + B^2 \pi_7^2 q^2} - \pi_7 C & p < -\pi_3 \end{cases}$
	$g(p, q, \boldsymbol{\pi}) = \begin{cases} \sqrt{(p + \pi_3)^2 \tan^2 \pi_6 + B^2 q^2} - C & p \geq -\pi_3 \\ \sqrt{(p + \pi_3)^2 + B^2 \pi_7^2 q^2} - \pi_7 C & p < -\pi_3 \end{cases}$
	$\pi_3 = (\pi_4 - \pi_7 \pi_5) / (1 + \pi_7 \tan \pi_6)$
	$A = \pi_8 / \cos \pi_6$
	$B = 1 / (1 + \pi_8 - A)$
	$C = \pi_5 + \pi_3 \tan \pi_6$
	$p_i = \pi_3 - \pi_8 C \sin \pi_6$

167 A single state variable (ϕ) is used in all constitutive models considered in the current work, which
 168 represents volumetric plastic strain in the VMDC and DPC models. The rate-form evolution law for this
 169 variable is given by Eq. 1,

$$\dot{\phi} = -\text{tr}(\mathbf{D}_p) = -d_p^v \quad (1)$$

170 where \mathbf{D}_p is the plastic rate of deformation tensor. In von Mises plasticity, the state variable instead
 171 represents equivalent plastic strain, and the evolution law is given by Eq. 2,

$$\dot{\phi} = \sqrt{\frac{2}{3} \mathbf{D}_p : \mathbf{D}_p} \quad (2)$$

172 In this work, following the results of the experimental work listed in the Introduction, elastic parameters
 173 and yield surface parameters are described as indirectly dependent on the state variable via the relative
 174 density, ρ_r (Eqs. 3a-3d),

$$\rho_r = \rho_{r0} e^{\phi} \quad (3a)$$

$$\boldsymbol{\pi} = \boldsymbol{\pi}(\rho_r(\phi)) \quad (3b)$$

$$E = E(\rho_r(\phi)) \quad (3c)$$

$$\nu = \nu(\rho_r(\phi)) \quad (3d)$$

175 In von Mises plasticity, relative density remains unchanged when plastic flow occurs, and elastic parameters
 176 and yield surface parameters are instead described as functions of equivalent plastic strain.

177 Compressible plasticity models where elastic moduli vary with plastic state variables have been im-
 178 plemented by several researchers (Cunningham et al., 2004; Diarra et al., 2018; Shang et al., 2012; Sinha
 179 et al., 2010; Sinka et al., 2003) using a method that combines an incremental elastoplasticity model with
 180 explicit update of elastic parameters based on volumetric plastic strain. In this work, a dedicated, fully
 181 implicit elastoplastic algorithm was used instead. This was implemented in the commercial finite element
 182 code Abaqus as a user-defined material subroutine (UMAT), allowing improved step-size convergence prop-
 183 erties over the explicit method. A full description of the algorithm and validation of the implementation is
 184 presented elsewhere (Edmans and Sinka, 2019).

185 3. Experimental identification of material parameters

186 3.1. General

187 A variety of methods are used to characterise the properties of granules. Although direct testing can
 188 be used to determine the material properties of compressible particles (for example, Chan et al. (2013)),
 189 such experiments are difficult to conduct and the results show high variation in properties between different
 190 samples. Conversely, instrumented die compaction is an established procedure for developing and calibrating
 191 constitutive models for simulating bulk powder compaction (see Sinka et al. (2001, 2003) or Cunningham
 192 et al. (2017) for examples). In the current work, it is assumed that values of the elastic modulus and
 193 hydrostatic yield strength obtained for powders in bulk using instrumented closed-die compaction tests are
 194 also valid for the particle material.

195 3.2. Nondimensionalisation

196 As the size and mechanical properties of engineering particles vary widely, it is useful to develop nondi-
 197 mensional parameters to enable equivalent simulations using different plasticity models to be conducted
 198 and results to be generalised. The subscript 0 will be used to indicate quantities describing a particle's
 199 initial state (before loading is applied). In this work, dimensionless quantities will be derived by dividing

200 by the hydrostatic yield stress in the initial state (σ_{y0}) for quantities with units of Nm^{-2} ; by the initial
 201 particle radius (R_0) for quantities with units of m; and by $\pi R_0^2 \sigma_{y0}$ for forces. Dimensionless quantities will
 202 be indicated by a superimposed bar. This nondimensionalisation enables a first-order characterisation of
 203 compressible plasticity models with three parameters, \bar{E}_0 , $\bar{\Gamma}_0$ and $\bar{\Lambda}_0$, representing initial elastic stiffness,
 204 initial maximum shear strength and initial tensile strength, respectively, together with the initial cap axis
 205 ratio ϵ_0 and parameter evolution expressions. It is noted that the parameters \bar{E} and $\bar{\Lambda}$ are functionally
 206 equivalent to the bulk parameters *strain index* and *bonding index*, respectively, introduced by [Hiestand and](#)
 207 [Smith \(1984\)](#) as tableting performance indicators. The relationship between generalised shape parameters
 208 and yield surface parameters specific to the plasticity models are given in Table 3.

209 3.3. A general parameter evolution model for particle material

210 Dimensionless strength and stiffness are assumed to have an exponential dependence on relative density,
 211 due to widespread use of such functions (see Introduction) and are described by the Eqs. 4a-4d,

$$\sigma_y(\rho_r) = \sigma_{y0} \exp(\eta(\rho_r - \rho_{r0})) \quad (4a)$$

$$E(\rho_r) = E_0 \exp(\xi(\rho_r - \rho_{r0})) \quad (4b)$$

$$\Gamma(\rho_r) = \Gamma_0 \exp(\zeta(\rho_r - \rho_{r0})) \quad (4c)$$

$$\Lambda(\rho_r) = \Lambda_0 \exp(\omega(\rho_r - \rho_{r0})) \quad (4d)$$

where the independent exponents η , ξ , ζ and ω are material parameters. Note that setting $\zeta = \omega = \eta$ will
 result in self-similar yield surfaces. In addition, the Poisson's ratio and compression cap axis ratio were
 prescribed to vary linearly with the relative density (Eqs. 5a-5b),

$$\nu(\rho_r) = \nu_0 + \xi_1(\rho_r - \rho_{r0}) \quad (5a)$$

$$\epsilon(\rho_r) = \epsilon_0 + \xi_2(\rho_r - \rho_{r0}) \quad (5b)$$

212 Accordingly, the VMDC and the DPC plasticity models can be described by twelve parameters: initial
 213 compressive yield strength (σ_{y0}), initial relative stiffness (\bar{E}_0), two initial yield surface shape parameters
 214 ($\bar{\Gamma}_0$ and $\bar{\Lambda}_0$), four evolution exponents (η , ξ , ζ and ω), four supplementary parameters (ν_0 , ϵ_0 , ξ_1 and ξ_2)
 215 and the reference relative density (ρ_{r0}). For the von Mises model, the initial deviatoric yield stress is used
 216 in place of the hydrostatic yield stress as a reference value and the exponent η prescribes its evolution.

217 3.4. Analysis of existing experimental data

218 The reference experimental data used in this work are primarily those published by [Cunningham et al.](#)
 219 [\(2017\)](#), who conducted instrumented die compaction tests on seven powders commonly used as pharmaceu-
 220 tical excipients, and [Bika et al. \(2001\)](#), who provided a survey of particle strength data including granules
 221 produced using both wet and dry agglomeration procedures. Data obtained from instrumented die com-
 222 paction tests are relevant to the industrial dry granulation processes of “roller compaction” and “slugging”,
 223 both of which involve dry agglomeration of powders under compression followed by milling. Generalised
 224 yield surface parameters and evolution parameters defined in the previous two subsections for granules tested
 225 by [Cunningham et al. \(2017\)](#) were inferred by extracting data points from the published charts using ScanIt
 226 (AmsterCHEM, 2018) and subsequent curve-fitting. The full set of material parameters found are presented
 227 in Table 4. Values of \bar{E}_0 obtained from [Bika et al. \(2001\)](#) are listed in Table 5. Values of \bar{E}_0 obtained from
 228 both articles are included in Fig. 2b.

229 3.5. Parameter space selected for numerical investigations

230 Numerical studies described in this work will focus on the VMDC model. Based on the experimental
 231 values listed in Section 3.4, a set of representative values was selected to implement in a VMDC model. This
 232 model is subsequently referred to as the *base case*. The values selected are listed in Table 6. Furthermore,
 233 the effects of varying the stiffness ratio (\bar{E}_0), shear strength ($\bar{\Gamma}_0$) and tensile strength ($\bar{\Lambda}_0$) were investigated.

234 The parameter space was designed to contain the envelope of parameters inferred from previous studies on
235 pharmaceutical excipients with respect to these three dimensionless measures. The parameter space chosen
236 for investigation was $[(\bar{E}_0, \bar{\Gamma}_0, \bar{\Lambda}_0) \in \mathbb{R}^3 : 3 \leq \bar{E}_0 \leq 500, 0.25 \leq \bar{\Gamma}_0 \leq 1, 0.01 \leq \bar{\Lambda}_0 \leq 1.0]$. This space is illus-
237 trated in Fig. 2. The range of stiffness values was selected as the envelope of experimental values (excluding
238 metallic powders). Values for shear and tensile strength were selected on the basis of the experimental data
239 presented by [Cunningham et al. \(2017\)](#), but in setting up the parameter space, it was considered that both
240 values were likely to be higher than those for compressed powders, as intraparticle forces are expected to
241 be stronger than interparticle forces if particle integrity is maintained when these two loading actions are
242 applied to an assembly.

Table 3

Generalised yield surface parameters for plasticity models.

Model	Yield surface parameters
VM	$\Gamma = \pi_2$
DPC	$\Lambda = \pi_5 / \tan \pi_6, \sigma_y = \pi_4, \Gamma = \pi_5 + \pi_3 \tan \pi_6, \epsilon = \pi_7$
VMDC	$\Gamma = \pi_2, \sigma_y = \pi_4, \Lambda = \pi_1, \epsilon = \pi_2 / (\pi_4 - \pi_3)$

Table 4

Material parameters, as determined from [Cunningham et al. \(2017\)](#). Initial values are presented at relative density $\rho_r=0.4$. Units of initial yield pressure (σ_{y0}) are MPa. *Negative values indicate that the linear model is inappropriate for $\rho_r=0.4$.

Material	σ_{y0}	\bar{E}_0	$\bar{\Lambda}_0$	$\bar{\Gamma}_0$	ξ_2	ϵ_0
Dical Emcompress	3.68	202	0.00149	1.139	0.844	0.455
Dical Fujicalin	28.2	36	0.0759	0.944	1.0222	0.645
Lactose DT	0.76	436	0.0925	1.141	1.006	0.304
Lactose 310 NF	0.33	500	0.00168	1.205	0.880	0.314
MCC PH-102	4.83	134	0.187	1.475	2.291	-0.0783*
MCC PH-200	8.61	51.3	0.0995	1.351	2.007	0.147
Starch 1500	1.49	335	0.00367	1.825	3.0364	-0.103*
Material	η	ξ	ω	ζ	ξ_1	ν_0
Dical Emcompress	9.94	9.82	19.80	18.66	0.367	0.15
Dical Fujicalin	8.25	9.92	5.91	4.86	0.362	0.147
Lactose DT	12.01	8.39	9.45	8.66	0.123	0.172
Lactose 310 NF	13.62	9.60	18.77	14.18	0.231	0.153
MCC PH-102	7.17	4.48	6.27	5.41	0.511	0.119
MCC PH-200	6.11	5.25	6.28	5.43	0.443	0.1472
Starch 1500	16.29	4.96	14.03	15.10	0.878	0.063

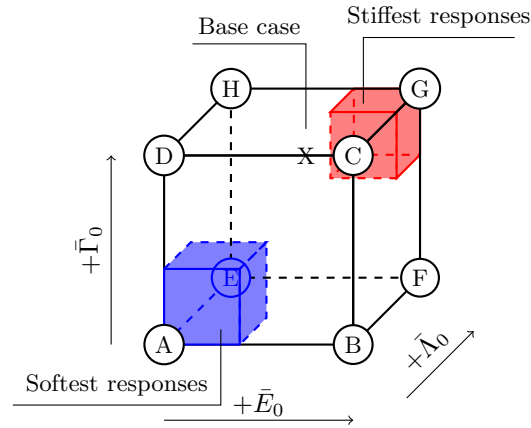
Table 5Values of \bar{E}_0 as determined from [Bika et al. \(2001\)](#)

Material	\bar{E}_0
Silanized glass beads, dry	344.8
Lactose monohydrate, dry	133.3
Monocrystalline cellulose, dry	163.9
Starch, dry	174.3
Alumina, sintered (5% strain)	1357.8
Alumina, sintered (20% strain)	1574.5
Glass beads w/ polyvinylpyrrolidone (PVP) binder	32.0
Silica sand w/ PVP binder	32.0
Lactose-Avicel-Starch w/ water binder	4.5
Lactose-Avicel-Starch w/ water/ethanol binder	5.3

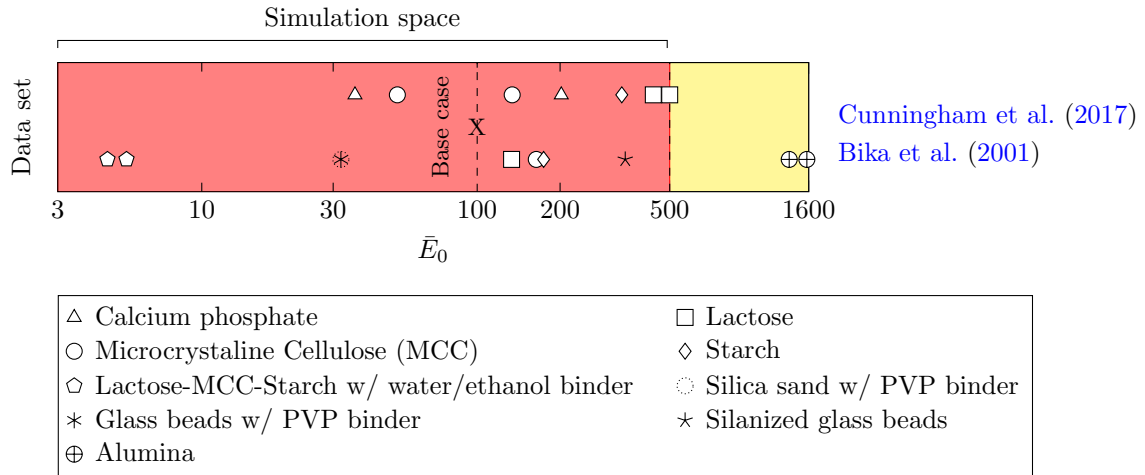
Table 6

Base case parameters for variable-stiffness VMDC model at $\rho_r=0.7$. Units of initial yield pressure (σ_{y0}) are MPa.

Material	σ_{y0}	\bar{E}_0	$\bar{\Lambda}_0$	$\bar{\Gamma}_0$	ξ_2	ϵ_0
Base case	150	100	0.01	1.0	1.5	0.7
Material	η	ξ	ω	ζ	ξ_1	ν_0
Base case	10	7.5	10	10	0.4	0.3



(a) Parameter space in \bar{E}_0 , $\bar{\Gamma}_0$ and $\bar{\Lambda}_0$



(b) Parameter space in \bar{E}_0 . Experimental data were obtained for dry compacted powders, unless binder is noted.

Fig. 2. The material parameter space considered, displayed using (a) Three dimensionless parameters (b) Dimensionless stiffness only.

243 4. Finite element modelling of particle contact

244 An axisymmetric model of a sphere in normal contact with a plane was created using the Abaqus/CAE
245 preprocessor. Taking advantage of symmetry, a half-sphere was modelled in contact with a rigid frictionless
246 plane. A uniform displacement boundary condition was applied to all nodes on the sphere midplane in the
247 vertical direction, leaving other degrees of freedom unconstrained, resulting in a configuration that is equiv-
248 alent to contact between two identical spheres. The mesh and boundary conditions used are shown in Fig.
249 3. 5372 triangular, axisymmetric (CAX3) elements of roughly equal size were used in an unstructured mesh.
250 The constitutive models described in Section 2 were implemented in a user-defined subroutine (UMAT),
251 enabling fully implicit integration of stresses and state variables, described elsewhere (Edmans and Sinka,
252 2019).

253 Contact was implemented using the “contact pairs” algorithm in Abaqus Standard. The Kuhn-Tucker
254 normal contact constraints were enforced directly and updated using the finite-sliding tracking algorithm.
255 The constraints were discretised using the “surface-to-surface” (mortar) method. A discrete rigid surface
256 was used to represent the contact symmetry plane, discretised with elements roughly half the size of the
257 elements used for the particle. Overpenetration was found to be negligible in all simulation results.

258 5. Numerical results

259 In this Section, qualitative and quantitative results obtained from FE simulations of particle contact
260 implementing the models described above are presented.

261 5.1. Load-displacement response for particles using different plasticity models

262 A comparison between the load-displacement response obtained from the base case VMDC simulation
263 and those obtained using other material models with equal stiffness and shear yield strength is shown in
264 Fig. 4. The Hertz solution (analytical elastic) and the elastic finite element solution (including geometric
265 nonlinearity) are included for reference. By inspecting Fig. 4, it can be seen that the difference between
266 responses obtained using the VMDC base case and the VM-perfectly plastic model lies in the hardening
267 behaviour and the existence of the tension and compression caps; shear behaviour is identical. The similarity
268 between the curves suggests that the presence of compaction hardening may not significantly affect the load-
269 displacement response, at least for small to moderate particle deformations and some parameter sets.

270 To investigate this further, a systematic study of differences between the VMDC and VM-PP models
271 in load predicted was conducted. Discrepancies between loads predicted by the two models for parameters
272 covering the entire parameter space (Fig. 2a) are shown in Fig. 6. These results show that the VM-
273 PP model significantly underestimates contact loads when stiffness, shear strength and displacements are
274 large. Differences are particularly sensitive to the value of the shear strength parameter $\bar{\Gamma}_0$. Fig. 6 can be
275 interpreted as a quantification of the influence of particle compressibility on load-displacement response: as
276 high compressibility implies low yield strength in compaction (high $\bar{\Gamma}_0$), the large positive errors noted in
277 these regions in Fig. 6 can be understood to result from compaction hardening. Conversely, discrepancies
278 are low at low values of $\bar{\Gamma}_0$. The shape of the yield approximates the VM surface more closely as $\bar{\Gamma}_0$, however
279 the behaviour of the two models does not become identical, even in the limit, as additional complexities
280 in behaviour are present in the VMDC models, such as the variable Poisson's ratio. Fig. 6 illustrates the
281 region of parameter space in which compaction hardening effects on particle load-displacement response are
282 significant, and a contact law developed using a compressible plasticity model, rather than the von Mises
283 model, should be employed.

284 5.2. Plastic zone development in particles for different plasticity models

285 Due to the use of compressible plasticity models, material points may exhibit different forms of yielding
286 behaviour depending on their stress state. In the VM-PP model, only deviatoric yielding is defined. In
287 the DPC model, distinct compaction and deviatoric yield behaviours are possible. In the VMDC model,
288 compaction, deviatoric ("shear") and tensile yielding are distinguished. Compaction yielding is associated
289 with an increase in material density and tensile yielding is associated with material dilation. For all fig-
290 ures in this Section, compaction, shear, tensile and elastic zones are coloured red, yellow, green and blue,
291 respectively. Fig. 7 shows the variation of the total particle volume undergoing each type of yielding with
292 time for simulations using the VMDC model with base case material parameters, and how this relates to
293 the force-displacement response.

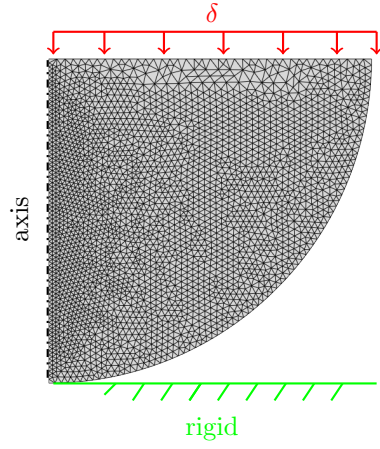


Fig. 3. Finite element mesh and boundary conditions used for sphere contact simulations

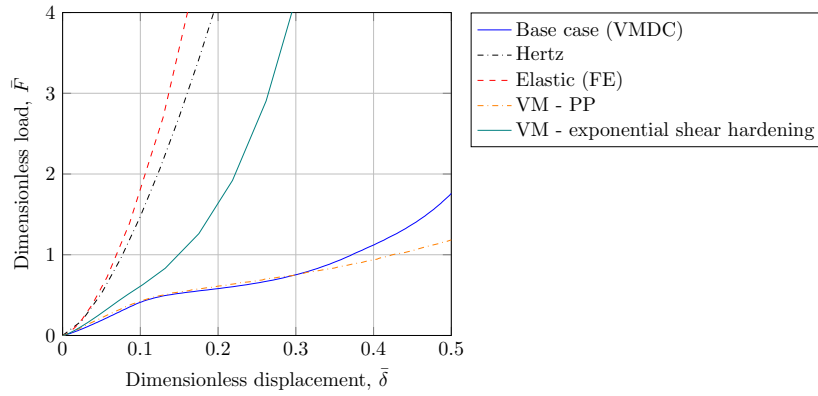


Fig. 4. Comparison of load-displacement responses between different models

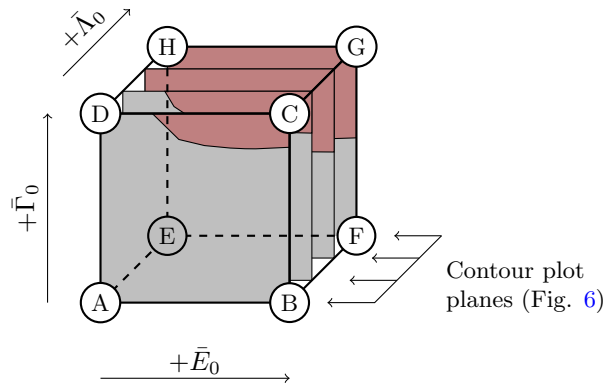


Fig. 5. Slices of parameter space shown in iso-discrepancy plots (Fig. 6). The upper right region in each slice indicates regions of the parameter space where the VMDC model predicts larger contact loads than the VM-PP model at $\bar{\delta} = 0.5$.

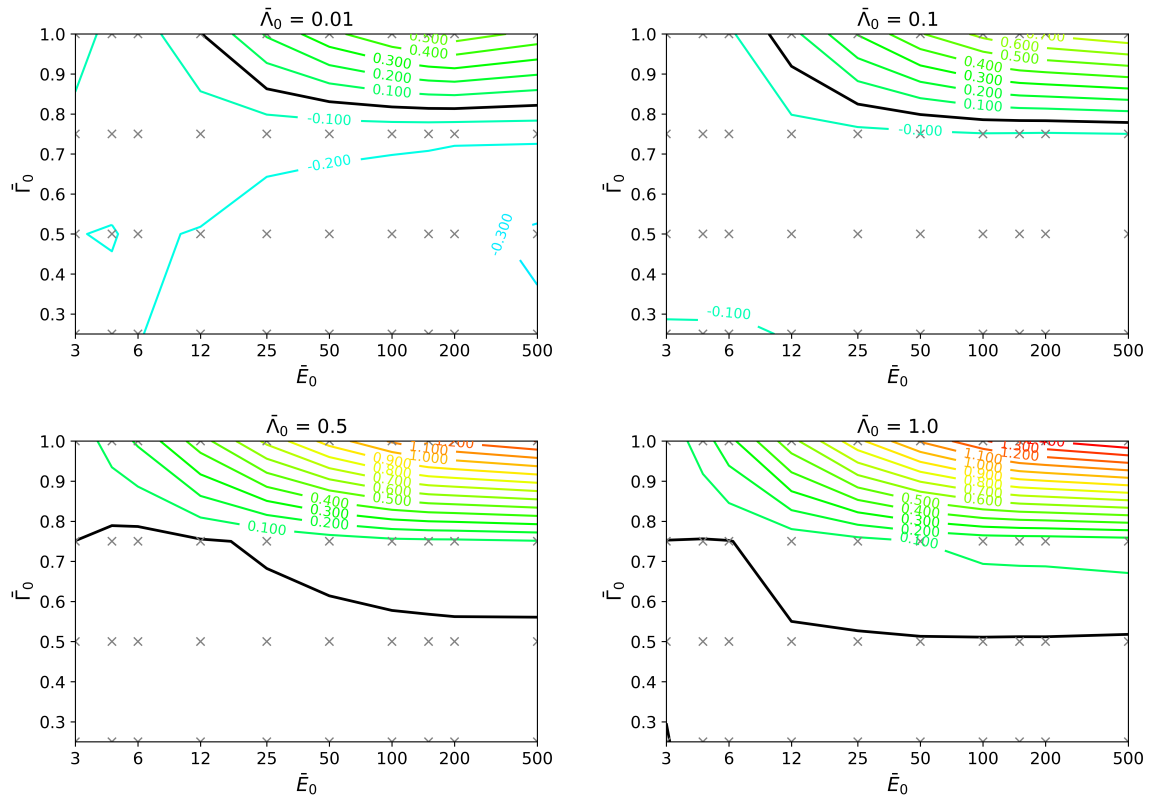


Fig. 6. Iso-discrepancy plots with respect to VM-PP load solution at maximum displacement ($\bar{\delta}=0.5$), showing influence of initial stiffness ratio \bar{E}_0 , initial shear strength ratio $\bar{\Gamma}_0$ and initial tensile strength ratio $\bar{\Lambda}_0$. Simulation points are marked with crosses (x). The thick black line defines the parameters where the force-displacement response predicted by the two models overlap. A logarithmic scale has been used on the stiffness axis for all plots.

Three distinct phases can be identified in the load-displacement response obtained using the VMDC material. The first, in which the load displacement response is roughly linear, is associated with rapid growth of a compaction zone at the point of contact (Fig. 8a). In the latter part of this phase (Fig. 8c), a dilation zone develops on the surface of the particle somewhat ahead of the contact zone. This zone expands into the interior and moves further ahead of the contact zone until it reaches the particle midplane. Before this point is reached, the effect of dilation on the force-displacement response is small because the regions affected are outside the load paths. Meanwhile, Poisson effects lead to large lateral tensile stresses developing near the particle midplane. This causes a transitional shear zone to develop between the elastic and compaction zones, and later, a secondary tensile zone at the midplane. Elasticity is dominant and the two tensile zones coalesce at the end of this phase.

In the second phase (Fig. 8e), the contact footprint and the dilation zone grow to such an extent that the force paths are disrupted, and the softening effect from dilation competes with the stiffening effect from compaction to reduce the stiffness of the particle response. The growth of the plastic zones is contained, but the zones gradually rearrange so that the load paths can be carried by strong channels of elastic and compacting material (Fig. 8g). This allows stiffening from compaction to progress more rapidly and the particle response stiffens again. The end of this phase is marked by the disappearance of all remaining elastic material.

In the third phase (Fig. 8i), two zones dominate: a compaction core consisting of all the material above the contact footprint, and a dilation zone outside this. The compaction zone only grows slowly in this phase and the dominant cause of the stiffening observed in the load-displacement response is the plastic hardening associated with increasing density of the material. Due to the exponential hardening of the material, the particle load-displacement response also approaches an exponential response asymptotically.

For comparison purposes, a simulation was carried out using the UMAT subroutine implementing the DPC model (with state-variable dependent elastic properties) with the same material parameters, using the equivalent yield surface concept illustrated in Fig. 1. A refined model with 21 030 elements was used to show plastic zone development more clearly. The load-displacement response and development of plastic zones is shown in Fig. 7. In distinction to the VMDC model, in the DPC model, the compaction zone remains small and the shear/dilation zone spreads from point just ahead of the compaction zones along the particle axis, and then spread out until about 85% of the whole particle is shearing when the simulation terminates (Fig. 8b, Fig. 8d, Fig. 8f, Fig. 8h and Fig. 8j). Failure occurs, at small values of $\bar{\delta}$, when the particle is unable to sustain additional tensile/shear load due to the prevalence of the yielded state. Stiffness of the response is 65% of the initial linear stiffness in the VMDC model (see Fig. 7). These results show that the shape of the yield surface in compressible plasticity models strongly influences particle behaviour. The patterns of yield zones shown by the simulations with the DPC model are qualitatively consistent with similar simulations carried out by Shang (2012) for a thin disk loaded across its diameter, which also used density-dependent parameters.

5.3. Plastic zone development in particles for VMDC parameter space

Comparisons between the proportion of the particle volume currently exhibiting each deformation mechanism and load-displacement for cases at the eight corners of the parameter space are shown in Fig. 9. The spatial development of plastic zones for these cases are shown in Fig. 10. These results show that widely different patterns of plastic deformation within particles (and associated micromechanics) can lead to similar load-displacement behaviour. This observation has the practical implication that force-displacement responses measured experimentally may be insufficient to characterise particle response, as they may hide a multitude of deformation mechanisms. This can be important because microstructure determines other properties of particles or granules, such as tensile strength. In several cases, regions exhibiting elastic behaviour reappear as deformation increases. This indicates the physical phenomenon of the stress state in these regions dropping below the yield surface temporarily until plastic flow resumes as loading increases. The high-frequency fluctuations in Figures 9e and 9f are numerical artefacts that arise in the computation of this phenomenon due to a number of elements exhibiting similar stress states. The oscillating nature of the flow states displayed by these elements can be appreciated by examining the instantaneous spatial distributions of flow behaviours shown in Fig. 10. For cases B and F, boundaries separating different flow

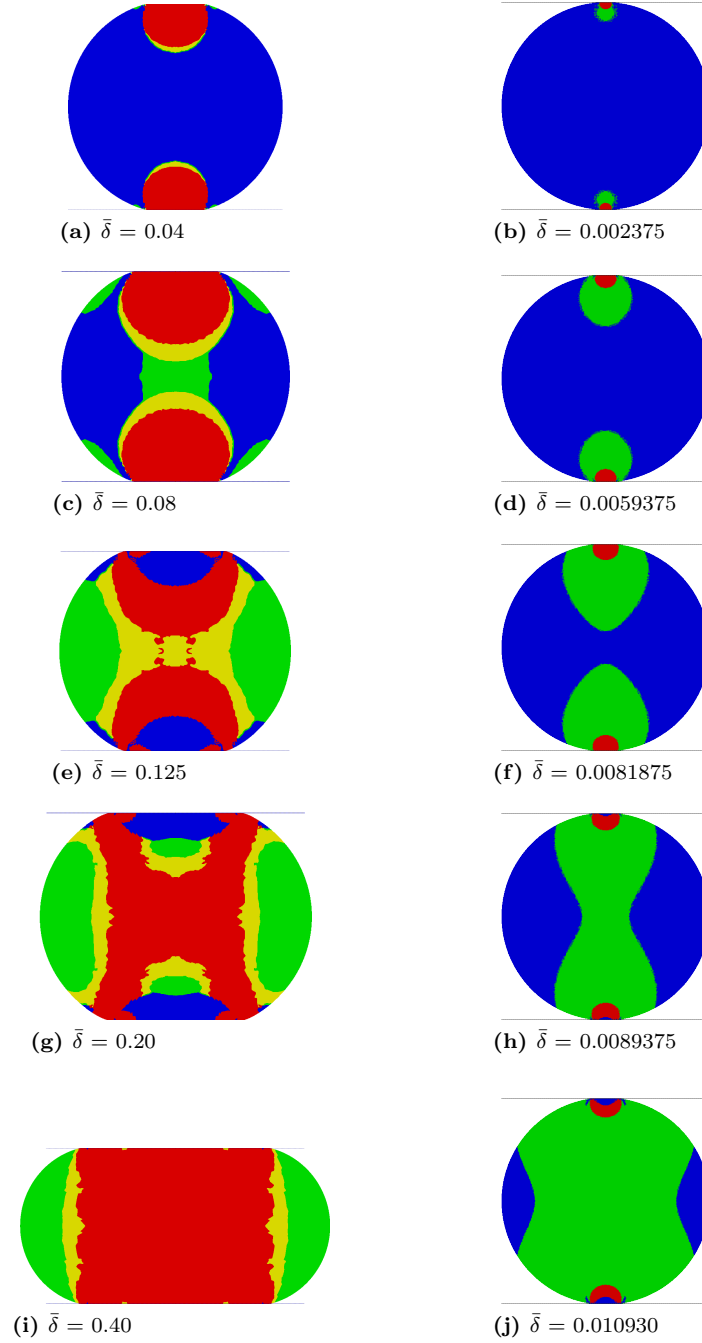


Fig. 8. Development of plastic zones in equivalent VMDC (left) and DPC (right) models, both with $\bar{E}_0=100$, $\bar{\Gamma}_0=1.0$, $\bar{\Lambda}_0=0.01$, and state variable-dependent elastic moduli. Colouring of plastic flow zones is as defined in Figure 7.

³⁴⁵ behaviours are less distinct than for the other cases. It is noted that no corresponding fluctuations are noted
³⁴⁶ in the load displacement response for these cases.

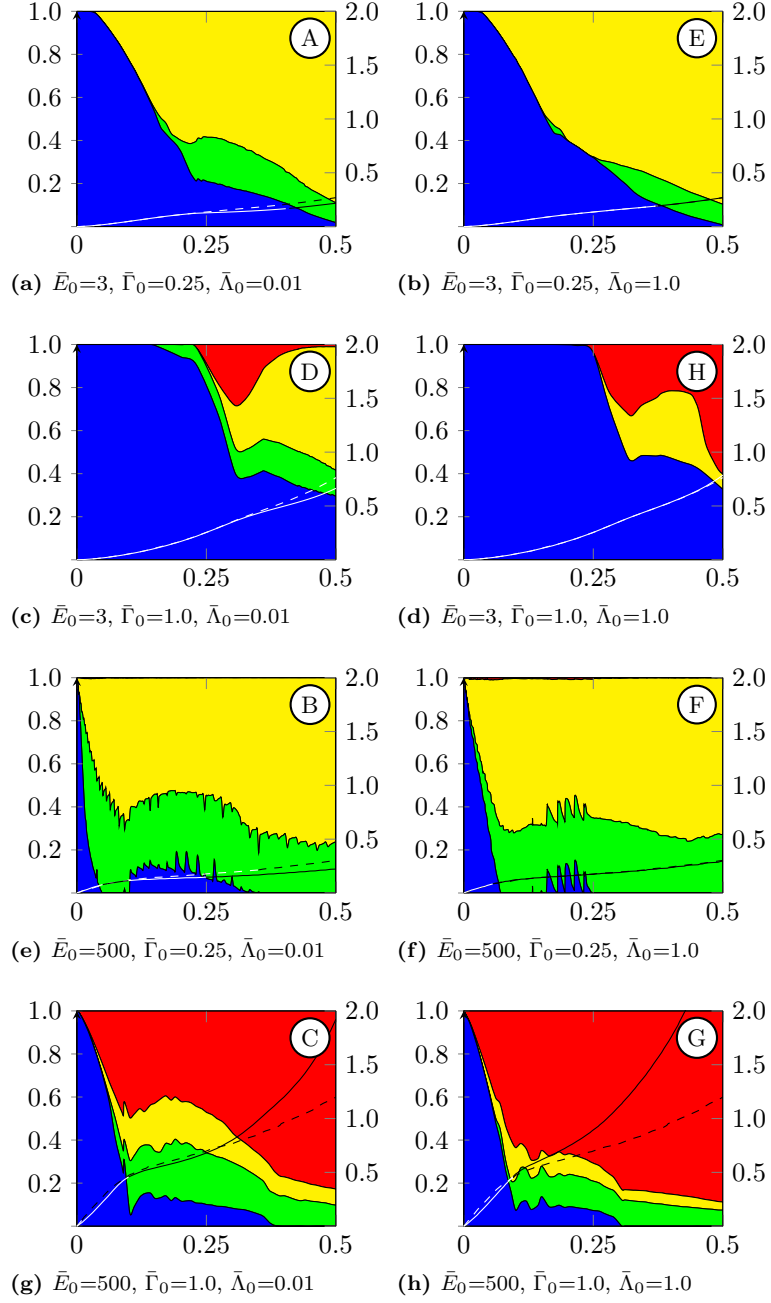


Fig. 9. Load-displacement response and development of volume proportion for deformation types at 8 corners of parameter space illustrated in Fig. 2a.

347 6. Contact law

348 6.1. Loading

349 Based on force-displacement simulation results and consideration of mechanisms, it is proposed that the
 350 force-displacement response of spherical particles behaving according to the VMDC material model can be
 351 represented by the following three-parameter contact law (Eq. 6),

$$\bar{F}_{model}(\bar{\delta}) = \begin{cases} k\bar{\delta}, & \bar{\delta} \leq \bar{\delta}_t \\ k\bar{\delta}_t \exp(a(\bar{\delta} - \bar{\delta}_t)), & \bar{\delta}_t < \bar{\delta} \leq \bar{\delta}_{max} \end{cases} \quad (6)$$

352 in which an initially linear response (corresponding to the first response phase described in Section 5.2) is
 353 combined with an exponential hardening response (corresponding to the second and third phases described
 354 in Section 5.2). As the range of applicability of this expression is limited by the source simulation data, the
 355 value of $\bar{\delta}_{max}$ is 0.5. The values of these parameters were determined for each load-displacement curve using
 356 a fitting procedure. The accuracy of this approximation was determined for each data set using the error
 357 area function (Eq. 7)

$$e_a = \frac{\left(\int_0^{\bar{\delta}_{max}} (\bar{F}_{model}(\bar{\delta}) - \bar{F}_{sim}(\bar{\delta}))^2 d\bar{\delta} \right)^{1/2}}{\int_0^{\bar{\delta}_{max}} \bar{F}_{sim}(\bar{\delta}) d\bar{\delta}} \quad (7)$$

358 and a peak error function (Eq. 8),

$$e_p = \max_{0 \leq \bar{\delta} \leq \bar{\delta}_{max}} (\bar{F}_{model} - \bar{F}_{sim}) / \bar{F}_{sim}(\bar{\delta}_{max}) \quad (8)$$

359 where \bar{F}_{sim} is the dimensionless load obtained from simulation.

360 Values of the contact law parameters were determined using a nested procedure. This procedure used an
 361 outer Newton-Raphson loop to find the area error-minimising value of $\bar{\delta}_t$, containing subroutines finding the
 362 best-fit parameters for each branch of Eq. 7 independently (by regression analysis) and return the area error.
 363 Cumulative error distributions for the fits obtained for all 160 simulations with this contact law are shown
 364 in Fig. 11, showing that median area error and maximum area errors are 0.388% and 3.96%, respectively.
 365 The worst, 90th percentile, 75th percentile and median cases for peak error are shown in Fig. 12a to Fig.
 366 12d, respectively.

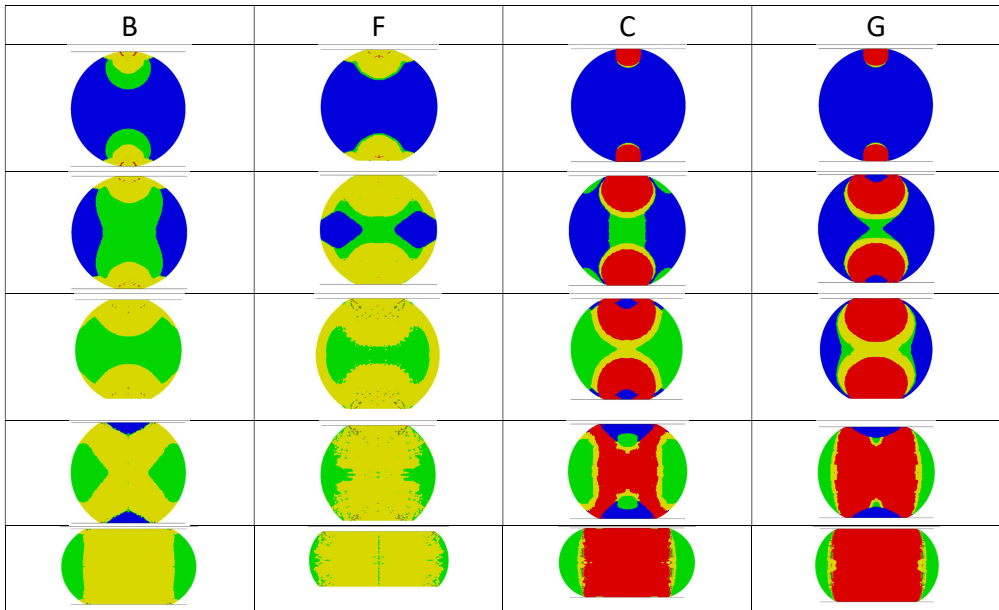
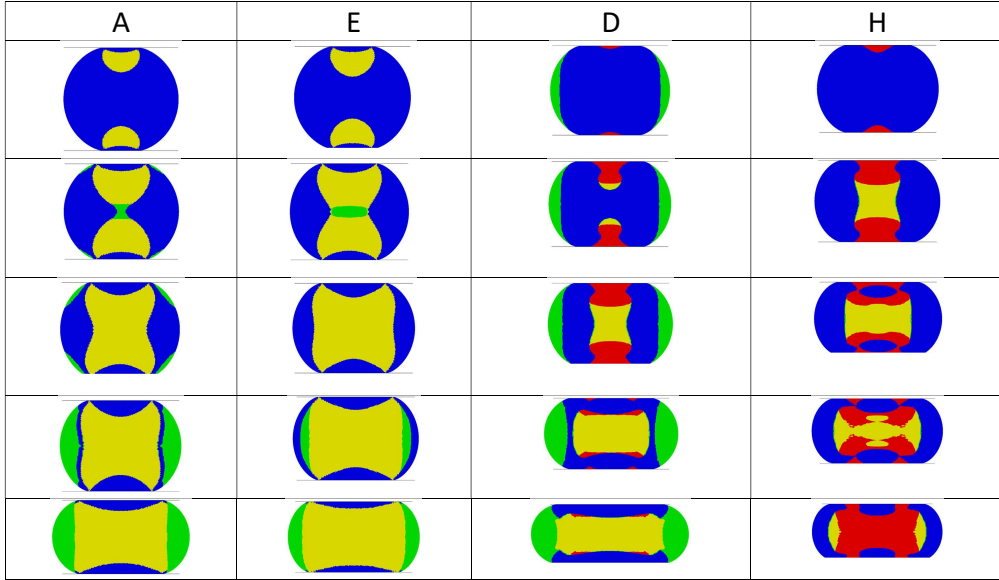


Fig. 10. Contact zone development. The spatial distribution of plastic flow zones are shown for the eight extreme combinations of material parameters \bar{E}_0 , $\bar{\Lambda}_0$ and $\bar{\Gamma}_0$ designated with the letters A-H in Fig. 2a. Plastic flow zones are shown at five successive intervals during particle compaction for each case.

367 *6.2. Yield surface shape study*

368 Sensitivity studies were carried out to determine the influence of material parameters of the particle
369 load-displacement response. The results indicated that Poisson effects (related to parameters ν_0 and ξ_1)
370 have little influence on the load-displacement response. The value of the stiffness evolution exponent ξ also
371 does not affect the results greatly. These two observations can be explained by noting that the particle
372 is unconstrained in the radial direction during compression and that once significant compaction/dilation
373 occurs, the response is dominated by plastic behaviour, and hence variation in the elastic modulus is less
374 important. Following this study, 6 material parameters are identified as having dominant influence on the
375 load displacement behaviour: the stiffness ratio (\bar{E}_0), the yield surface shape parameters ($\bar{\Gamma}_0$ and $\bar{\Lambda}_0$), the
376 compressive hardening exponent (η) and the cap shape parameters (ϵ_0 and ξ_2).

377 Following the sensitivity study, a systematic study was carried out to determine the influence of the
378 stiffness ratio \bar{E}_0 and initial yield surface shape parameters $\bar{\Lambda}_0$ and $\bar{\Gamma}_0$ on the parameters of the contact law.
379 These parameters were selected for the study due as they are easiest to determine experimentally. Sphere
380 contact simulations were carried out for all combinations $\bar{E}_0 = 3, 4.5, 6, 12, 25, 50, 100, 150, 200, 500$;
381 $\bar{\Lambda}_0 = 0.01, 0.1, 0.5, 1.0$ and $\bar{\Gamma}_0 = 0.25, 0.5, 0.75, 1.0$, resulting in 160 simulations. The distribution of errors
382 between the fitted contact law and the results from these simulations is shown in Fig. 11, where it can be
383 seen that the median peak error in \bar{F} is 1.955% and the median area error (as defined by Eq. 7) is 1.03×10^{-4} .
384 The variation of the contact law parameters with the material parameters is shown in Figs. 13a - 13c.

385 In general, these results show that the influence of particle shear strength ($\bar{\Gamma}_0$) is relatively strong while
386 that of the tensile strength ($\bar{\Lambda}_0$) is relatively weak, and this is true for contact law parameters governing both
387 the initial linear response (Fig. 13a) and the later exponential region (Fig. 13b). Secondly, the hardening
388 exponent a decreases sharply between $\bar{\Gamma}_0=1.0$ and $\bar{\Gamma}_0=0.75$. By inspecting the development of contact zones
389 in these models, it can be seen that the formation of the “double-cone” structure of compacted material
390 noted in Section 5.2 is only achieved briefly when $\bar{\Gamma}_0=0.75$; the structure is absent at the end of the loading,
391 which inhibits the particle hardening response.

392 In order to use the contact law and unloading law for DEM of compressible particles, material parameters
393 can be determined experimentally and k , δ_t and a can be interpolated from Figs. 13a, 13b and 13c,
394 respectively. Relations allowing the direct prediction of contact law parameters from material parameters
395 were derived using regression analysis, the results of which are shown in Appendix A.

396 *6.3. Unloading*

397 Unloading of plastically deformed spheres is predominantly elastic but nonlinear. Load-displacement
 398 relations for unloading of spherical particles which have undergone plastic deformation have been proposed
 399 by [Kogut and Etsion \(2002\)](#), as well as several other investigators. However, almost all studies are limited
 400 to predicting unloading behaviour where displacements ($\bar{\delta}$) are small, and consequently are not applicable to
 401 the particle deformation scenarios explored in the finite element simulations carried out in the current work.
 402 Results from simulations of unloading from large displacements are shown by [Li et al. \(2009\)](#); however, the
 403 authors do not provide an explicit force-displacement relation.

To formulate a contact law for general unloading processes, separate parameters representing the nonlin-
 earity of the unloading curve and the relative unloading stiffness were defined. It is assumed that unloading
 follows a power-law model (Eq. 9),

$$\bar{F}_{unl}(\bar{\delta}) = \begin{cases} 0, & \bar{\delta} \leq \bar{\delta}_0 \\ k(\bar{\delta} - \bar{\delta}_0)^\alpha, & \bar{\delta} > \bar{\delta}_0 \end{cases} \quad (9)$$

404 subject to the boundary condition $\bar{F}_{max} = \bar{F}_{unl}(\bar{\delta}_{max})$, where $\bar{\delta}_0$ is the nondimensionalised displacement
 405 at separation. Classical Hertzian unloading is recovered as a special case of Eq. 9, where the nonlinearity
 406 factor α is 1.5 and k is given by Eq. 10,

$$k = k_H = \frac{4}{3\pi} \left(\frac{\bar{E}_0}{1 - \nu_0^2} \right) \quad (10)$$

407 Relative unloading stiffness can be quantified using the secant stiffness ratio β , defined with Eq. 11,

$$\beta = \frac{\bar{\delta}_{max} - \bar{\delta}_{H0}}{\bar{\delta}_{max} - \bar{\delta}_0} \quad (11)$$

408 where the displacement at separation predicted by the Hertz model, $\bar{\delta}_{H0}$ obtained when unloading from the
 409 same final load, \bar{F}_{max} , can be calculated using Eq. 12,

$$\bar{\delta}_{H0} = \bar{\delta}_{max} - \left(\frac{\bar{F}_{max}}{k_H} \right)^{2/3} \quad (12)$$

410 In Fig. 14, sample unloading curves defined by Eq. 9 with varying α and constant β are illustrated.

411 By substituting the unloading law into the boundary condition, the unloading law can be expressed in
 412 terms of the maximum load (Eq. 13).

$$\bar{F}(\bar{\delta}) = \begin{cases} 0, & \bar{\delta} \leq \bar{\delta}_0 \\ \bar{F}_{max} \left(\frac{\bar{\delta} - \bar{\delta}_0}{\bar{\delta}_{max} - \bar{\delta}_0} \right)^\alpha, & \bar{\delta} > \bar{\delta}_0 \end{cases} \quad (13)$$

413 A two-dimensional nonlinear least-squares regression was used to determine the parameters α and $\bar{\delta}_0$ for
 414 each unloading curve that minimised errors between the model and the data. This procedure resulted in
 415 values of the coefficient of determination (R^2) with a minimum of 0.998825 and median of 0.999948 across
 416 all 160 load cases. The stiffness k can then be determined using Eq. 14,

$$k = \frac{\bar{F}_{max}}{(\bar{\delta}_{max} - \bar{\delta}_0)^\alpha} \quad (14)$$

417 Results for α and β for the unloading curves for the eight corners of the parameter space are shown in Figs.
 418 15a and 15b, respectively. Results for large-displacement elastic unloading and unloading from simulations
 419 using the VM-PP model are included for reference.

420 The unloading stiffness of particles depends conceptually on both properties of the particle material and
 421 influences related to the geometry of deformation (itself related to material properties). It is evident from
 422 Figs. 15a and 15b that widely different values unloading stiffness (β) are obtained for different materials
 423 with the same degree of particle deformation ($\bar{\delta}$). Furthermore, this difference is not explained by different
 424 values of contact radius (\bar{a}) arising in different simulation for a given value of $\bar{\delta}$, as similar values of \bar{a} are
 425 obtained for simulations with different \bar{E}_0 but identical $\bar{\delta}$ (Fig. 16). Considering first unloading from a
 426 nonlinear elastic simulation, it can be seen that both the power-law exponent and secant stiffness ratio
 427 increase at large deformations, which results from the increasing inaccuracy of the assumptions of the Hertz
 428 model as deformation increases. Results from VM-PP simulations tend towards those for the nonlinear
 429 elastic response as \bar{E}_0 decreases, and becomes identical when \bar{E}_0 is low enough that no yielding occurs.
 430 Conversely, where \bar{E}_0 is large, nonlinearity in the unloading response is reduced and unloading stiffness (β)
 431 is significantly higher than that predicted by the Hertz law, even though no increase in the material stiffness
 432 has occurred. This reduction in α was also noted by Etsion et al. (2005) (Eq. 17); no dependence on \bar{E}_0
 433 is present in this version of the relation as an alternative nondimensionalisation is used that obscures the
 434 effect. In addition, the fact that these authors observe a decrease rather than an increase in nonlinearity,
 435 as is observed in the results presented in Figure 15b, may be explained that the former were obtained from
 436 simulations with relatively high values of \bar{E}_0 (297-2464). An additional cause is suggested by results from
 437 Jackson and Green (2005) (Fig. 6), which suggest that average contact pressure increases rapidly in the
 438 initial stages of contact to maximum value of about 3, then decreases at high displacements to 1, whereas
 439 in the simplified model, a value of only 1 is approached asymptotically.

440 Trends in results for the simulations using the VMDC model are similar to those obtained with the VM-
 441 PP model at equal \bar{E}_0 . Results from cases G and C show that the effect of increase in elastic modulus due
 442 to compaction on unloading stiffness is negligible, despite the large degree of compaction exhibited by the
 443 particle in these cases. Values obtained for the secant stiffness ratio for cases with reduced shear strength
 444 (A, E, B, F) are significantly larger than other results with equivalent \bar{E}_0 . It is therefore proposed that
 445 the relevant stiffness ratio that influences shear unloading is $E/\sigma_{y0}^{VM} = \bar{E}_0/\bar{\Gamma}_0$ rather than \bar{E}_0 , which is 12
 446 rather than 3 for these cases.

447 In summary, the nondimensionalised displacement ($\bar{\delta}$) before unloading and the shear stiffness ratio
 448 ($\bar{E}_0/\bar{\Gamma}_0$) are found to be the most significant material parameters determining unloading stiffness. However,
 449 a fuller explanation of the effects shown in Fig. 15b and formulation of an explicit relation between material
 450 parameters and parameters of the contact law in the large-displacement unloading regime is left for future
 451 work.

452 7. Discussion

453 The modelling approach described in this article relies on the assumption that the response to mechanical
454 loading of a compressible particle can be described by a continuum, isotropic, elastoplastic constitutive law
455 with initially homogeneous properties. Two issues may be distinguished in relation to this assumption:
456 firstly, the degree of continuity and homogeneity of the particle's initial state, and secondly, the influence
457 of crack initiation and growth during particle deformation. Regarding the first issue, there is extensive
458 literature in the field of granulation showing how the overall density of produced granules as well as their
459 microstructure can be modified by controlling the granulation process type and process parameters. The
460 internal structure of the granules can vary between extremes of hollow shells to granules with uniform
461 porosity. Greater density can result in the outer regions of manufactured granules. It has been shown that
462 it is possible to engineer compacts with different internal density distributions and how this affects their
463 strength as measured using standard mechanical testing. The particle contact simulations described in the
464 current work could be used to investigate the effects of initial density distributions; however, this is left for
465 future work. A recent review and discussion of pore structure and influence on mechanical properties relevant
466 to this issue is provided by [Markl et al. \(2018\)](#). Regarding the second issue, the growth of microscopic cracks
467 under load could lead to brittle fracture at lower loads than the maximum loads obtained in the simulations
468 carried out in this work. For example, single particle compression tests on 0.8mm diameter microcrystalline
469 cellulose (a relatively ductile pharmaceutical excipient) particles by [Che \(2017\)](#) found that the average value
470 of $\bar{\delta}$ when fracture occurred was 0.225. Maximum tensile principal stress is widely used as a criterion for
471 failure due to cracking in continuum models. By predicting the deformation at which such a criterion is
472 reached, the models described in this work could be used to relate particle material properties to particle
473 strength, and explore the accuracy in predicting failure of different criteria in particles of varying ductility.
474 The locations of crack initiation predicted by this model could be compared with experimental findings.
475 The maximum deformation of $\bar{\delta} = 0.5$ used in this work should cover most practical scenarios.

476 The proposed contact law is presented in a form ready for DEM implementation for simulation of multi-
477 particle systems. For dense systems, the realism of the assumption of independence of contact interactions
478 should be considered.

479 The findings of this work can be compared with empirical efforts at establishing performance indices
480 by [Hiestand and Smith \(1984\)](#), which describe powder behaviour at the bulk level. These authors argued
481 that the ratio of elastic stiffness to deviatoric yield limit E_0/σ_{y0}^{VM} should influence the strength of compacts
482 because it arises in the expression for strain energy release rate that governs crack growth in classical linear
483 elastic fracture mechanics theory, though later work concludes that its potential domain of influence is
484 restricted to when values are low, as plastic deformation dominates in practical die compaction ([Hiestand,
485 1997](#)). The current work suggests that the stiffening in the particle load-displacement response noted with
486 increase in \bar{E}_0 should influence powder compactability. Future experimental work would be needed to
487 quantify the relative importance of influences of \bar{E}_0 on inter-particle bonds and particle internal bonds
488 during bulk compaction; results by [Johansson and Alderborn \(1996\)](#) suggest that the latter is of more
489 importance, at least for ductile particles.

490 The distinction between continuum material models for describing granular assemblies and those used
491 as homogenised representation of compressible particles should be emphasised. It is typically assumed that
492 the bulk behaviour of powders undergoing compaction can be described by standard compressible plasticity
493 models, such as the popular Drucker-Prager Cap model. However, direct application of such models to the
494 particle level is not straightforward, as shear forces acting between particles differ in strength and nature
495 from those acting between the sub-particles within them, with the former resulting from adhesion and friction
496 mechanisms and the latter from liquid and solid bridges. The numerical exploration of different compressible
497 plasticity models carried out in the current work suggests that the VMDC yield surface is more realistic for
498 modelling particle material mechanical behaviour than the DPC surface, as the latter predicts that particle
499 limit loads will occur at much lower levels than in practice, for fixed values of initial tensile, shear and
500 compressive yield strength. This in turn suggests that bonding within compressible particles is closer to the
501 isotropic bonding that exists in sintered metals than the pressure-dependent frictional interactions implied
502 by the DPC model. The future development of experimental techniques for direct or indirect determination

503 of compressible particle properties may help establish the extent to which this is the case.

504 Use of more sophisticated and direct parameter characterisation methods for the particle material model
505 would increase the utility of the current work. It is not possible to uniquely assign a material model to a
506 particle or determine its parameters on the basis of particle uniaxial load-displacement data alone. As can be
507 seen from Figure 6, the shear strength (Γ_0) has strong influence on the particle stiffening. A proposed first
508 step for further investigation could be to investigate the load-displacement response of a single particle under
509 diametral compression loading to establish and quantify the extent of material densification and hardening
510 (from Figure 4, it can be seen that some particle hardening is observed even without material hardening).
511 Next, an estimate of shear strength could be made using microscopic inspection of the internal deformation
512 of deformed particles. More accurate estimates of particle material properties could be achieved with other
513 testing methods, such as triaxial testing apparatus for single particles. The authors believe that this type of
514 apparatus is most suited to investigate material properties of granules and validate the contact law developed
515 in this work. As these tests do not induce uniform stress states in the particles, these tests would still provide
516 indirect estimates for the material yield points that might need further simulations to interpret. For particles
517 whose internal structure is well understood, it might be possible to prepare larger samples with equivalent
518 density and structure to the corresponding particles, and use standard triaxial testing techniques.

519 The simulations conducted in this work do not include friction as they are intended to represent normal
520 contact between two identical particles. Frictional forces do not arise in this configuration as there is no dif-
521 ference in the radial displacement fields between the two particles. However, if experiments were conducted
522 to validate the contact law by crushing a particle between two platens, friction would arise, necessitating
523 inclusion of a friction model in the corresponding numerical simulation. In this context, especially when
524 large particle deformations occur, frictional effects may become relevant as friction restricts particle lateral
525 deformation and, via Poisson effects, increases normal elastic stiffness. Similarly, in yielding material, this
526 constraint could cause the hydrostatic component of the the stress to increase, leading to more rapid densifi-
527 cation and particle stiffening. This effect has been noted in the different stress states observed in unconfined
528 uniaxial compression and closed-die compaction of powders (see, for example, [Shang et al. \(2012\)](#), Figure
529 1b). Frictional effects have been ignored in the current work for several additional reasons: (1) its effect
530 was judged to be secondary to those of the stiffness and strength ratios; (2) it is difficult to quantify for
531 real particles and more complicated still to relate to invariant properties of the particles as it depends on
532 a number of factors: particle shape; surface roughness/asperity radius; surface chemistry and presence of
533 adsorbion layer; and presence of moisture or lubrication (3) it can introduce numerical problems of conver-
534 gence and mesh distortion, though these can be addressed by using alternative discretisation approaches,
535 such as the Material Point Method ([Li et al., 2009](#)). The authors believe that, at the current stage of
536 development, it is more important to focus on the exploring the effect of the three most important ma-
537 terial factors (stiffness:yield strength, shear strength:compressive strength and tensile:compressive strength
538 ratios) on the contact law. The determination of contact laws describing relationships between tangential
539 deformation/sliding and tangential loading is also desirable but outwith the scope of the current work.

540 8. Conclusions

541 In this work, the response of particles displaying irreversible deformation under contact was investigated.
542 This was achieved by carrying out finite element simulations using a spherical particle geometry under
543 the assumption that the mechanical response of the interior can be assumed to be homogenous and can
544 be described by continuum flow plasticity models. In order to achieve this, a new constitutive law, the
545 VMDC model, was introduced, which separates compressive, deviatoric and dilatatory plastic behaviour,
546 and incorporates both plastic hardening and increase of elastic moduli with material densification. A
547 fully implicit scheme (details described elsewhere ([Edmans and Sinka, 2019](#))) was used to integrate the
548 constitutive law. Parameters used for the VMDC model in the studies described in this article were based
549 on experimental data obtained for a range of granular materials, supporting the thesis that the trends and
550 mechanisms discovered are applicable to real particles, with a wide range of properties, used in different
551 industries. Given the generality of the VMDC model proposed, the qualitative findings of this work should
552 also be applicable to particles with material behaviour described by other compressible plasticity models.

553 The primary result of this work is a new contact law (Eqns. 6 and 9) and methods for relating parameters
554 of the contact law to material parameters, which is presented as a contribution in the field of contact
555 mechanics and suitable for implementation in discrete element codes. To the authors' knowledge, this is
556 the first contact law that describes the behaviour of plastically compressible particles. The contact law
557 is particularly useful for the analysis of dense particulate systems where individual particles are subject
558 to large deformations under compressive, tensile and shear conditions. By mapping an extensive material
559 parameter space, this work identifies the set of parameters for which material densification dominates the
560 force-displacement response. In addition, results were obtained concerning (1) the spatial development of
561 regions exhibiting distinct plastic flow behaviours; (2) the displacement range and region of parameter space
562 in which the differences in load-displacement response with that predicted using a metal plasticity model
563 become significant, and (3) the influence of material parameters on unloading stiffness and nonlinearity.
564 Results in these three categories should be generalizable to non-spherical particles, though this remains to
565 be shown.

566 The following relationships between material parameters and contact law parameters for VMDC materials
567 were found:

- 568 • Increasing material stiffness (\bar{E}_0) leads to increased initial linear stiffness in the particle response (k)
569 as expected (Fig. 13a), as unyielded material is most widespread in the response regime covered by
570 the initial segment of the contact law (Eqn. 6). However, this effect is modest compared with the
571 magnitude of the increase of material stiffness.
- 572 • The shear strength ($\bar{\Gamma}_0$) has a strong positive influence on the rate of hardening (a) of the particle
573 at large displacements (Fig. 13b). This occurs because zones of compacted material become smaller
574 when the shear strength is reduced. As shown in Fig. 10 compacted zones are surrounded by wide
575 regions of shearing material. As discussed later, hardening of the particle response is dependent on
576 the establishment of stable load paths transmitting the contact loads on the particle.
- 577 • Both the shear strength ($\bar{\Gamma}_0$) and tensile strength ($\bar{\Lambda}_0$) contribute positively to the particle stiffness,
578 but the shear strength is significantly more important (Fig. 13a - Fig. 13c). The lower the tensile or
579 shear strength is relative to the compressive yield strength, the greater the proportion of the particle
580 volume that yields according to the associated mechanism.
- 581 • The parameter $\bar{\delta}_t$ represents the deformation at which transition between the linear and exponential
582 terms of the contact law is centred. Fig. 13c shows that increasing stiffness (\bar{E}_0) leads to an earlier
583 transition because yielding occurs at smaller strains.

584 Results from the finite element simulations were also employed to examine the interaction of internal
585 loads developed to carry the contact pressure load. The results (shown in Fig. 9) indicate that the stiffness
586 to yield strength ratio, (widely used as a criterion for characterising particles as “elastoplastic” or “plastic”
587 in response) retains its importance when compressible plasticity models are used, and governs the proportion
588 of the particle that remains in the elastic state. Conversely, the influence of the ratio of tensile strength
589 to compressive strength is relatively weak, which is understandable as the loading and geometry tends to
590 distribute loads such that hydrostatic pressure becomes tensile only near the two points on the particle
591 circumference furthest from the contact points. The results also indicate that plastic deformation of the
592 particle may additionally be characterised as “metallic” or “compacting”, depending on the proportion of
593 material that exhibits deviatoric and compressive plastic flow, respectively. Results from the parametric
594 studies indicate that a high ratio of shear strength to compressive strength is necessary for the development
595 of connected regions of continually compacting material, which is a prerequisite for the realisation of the
596 hardening capacity of the particle material. For general yield surfaces, this sensitivity suggests that more
597 accurate representations of the compaction segment of a yield surface, established by experiments that
598 probe the yield surface at several points, may be required to make reliable predictions regarding the load-
599 displacement response of compressible particles. Fig. 10 illustrates the development of compacted regions
600 clearly: in cases A, E, B and F, a connected region of compacted material never develops; in cases C and G,

601 the development is robust; in case D, development aborts; and in case H, the development is interrupted by
602 the development of a central zone of shearing material, but later recovers. This spatial aspect suggests that
603 it might be possible to engineer porous particles with a small, low-density (or otherwise weakened) core in
604 order to reduce required compaction loads without reducing the tensile strength of the compacts produced.

605 As shown in Figures 4, 6, 9h and 9d, load-displacement responses remain close to those predicted from
606 simulations using a classical metal plasticity material model, up to displacements of at least $\bar{\delta} = 0.1$ in the
607 cases tested, even when an appreciable quantity of the material is compacting. However, significantly stiffer
608 responses may be obtained when stiffness ratio and shear strength ratio are high, and displacements are
609 large. These results indicate the condition when use of a contact law considering compressibility, rather
610 than one derived from a metal plasticity model, should be considered.

611 Acknowledgements

612 This work was supported by the UK Engineering and Physical Science Research Council (project reference
613 EP/N025261/1).

References

- Alcalá, J., Esqué-de los Ojos, D., 2010. Reassessing spherical indentation: Contact regimes and mechanical property extractions. *International Journal of Solids and Structures* 47, 2714–2732. doi:[10.1016/j.ijsolstr.2010.05.025](https://doi.org/10.1016/j.ijsolstr.2010.05.025).
- Barrera-Medrano, D., Salman, A.D., Reynolds, G.K., Hounslow, M.J., 2007. Granule Structure, in: *Granulation*. Elsevier, chapter 25, pp. 1189–1212. doi:[10.1016/S0167-3785\(07\)80060-1](https://doi.org/10.1016/S0167-3785(07)80060-1).
- Bika, D.G., Gentzler, M., Michaels, J.N., 2001. Mechanical properties of agglomerates. *Powder Technology* 117, 98–112. doi:[10.1016/S0032-5910\(01\)00318-7](https://doi.org/10.1016/S0032-5910(01)00318-7).
- de Boer, R., Brauns, W., 1990. Kinematic hardening of granular materials. *Ingenieur-Archiv* 60, 463–480. doi:[10.1007/BF00531256](https://doi.org/10.1007/BF00531256).
- Borja, R.I., 1991. Cam-Clay plasticity, Part II: Implicit integration of constitutive equation based on a nonlinear elastic stress predictor. *Computer Methods in Applied Mechanics and Engineering* 88, 225–240. doi:[10.1016/0045-7825\(91\)90256-6](https://doi.org/10.1016/0045-7825(91)90256-6).
- Chan, S., Wang, S., Lai, C., Grosso, J., 2013. A new perspective on the mechanical evaluation of granular material. *Drug Development and Industrial Pharmacy* 39, 1126–1132. doi:[10.3109/03639045.2012.715353](https://doi.org/10.3109/03639045.2012.715353).
- Chang, C.S., Gao, J., 1995. Second-gradient constitutive theory for granular material with random packing structure. *International Journal of Solids and Structures* 32, 2279–2293. doi:[10.1016/0020-7683\(94\)00259-Y](https://doi.org/10.1016/0020-7683(94)00259-Y).
- Che, L., 2017. Numerical constitutive laws for powder compaction using particle properties and packing arrangement. Ph.D. thesis. University of Leicester.
- Coulomb, C.A., 1776. Essai sur une application des règles de maximis et minimis à quelques problèmes de statique, relatifs à l'architecture. *Mem. Acad. Roy. Div. Sav.* 7, 343–387.
- Cundall, P., Strack, O., 1979. A discrete numerical model for granular assemblies. *Géotechnique* 29, 47–65. doi:[10.1680/geot.1979.29.1.47](https://doi.org/10.1680/geot.1979.29.1.47).
- Cunningham, J., LaMarche, K., Zavaliangos, A., 2017. Modeling of powder compaction with the Drucker-Prager cap model, in: Pandey, P., Bharadwaj, R. (Eds.), *Predictive Modeling of Pharmaceutical Unit Operations*. Woodhead Publishing, pp. 205–227. doi:[10.1016/B978-0-08-100154-7.00008-9](https://doi.org/10.1016/B978-0-08-100154-7.00008-9).
- Cunningham, J., Sinka, I., Zavaliangos, A., 2004. Analysis of tablet compaction. I. Characterization of mechanical behavior of powder and powder/tooling friction. *Journal of Pharmaceutical Sciences* 93, 2022–2039. doi:[10.1002/jps.20110](https://doi.org/10.1002/jps.20110).
- Dassault Systèmes, 2014. *Abaqus Theory Guide*. Providence, RI, USA.
- Diarra, H., Mazel, V., Busignies, V., Tchoreloff, P., 2018. Sensitivity of elastic parameters during the numerical simulation of pharmaceutical die compaction process with Drucker-Prager/cap model. *Powder Technology* 332, 150–157. doi:[10.1016/j.powtec.2018.03.068](https://doi.org/10.1016/j.powtec.2018.03.068).
- Drucker, D.C., Prager, W., 1952. Soil mechanics and plastic analysis for limit design. *Quarterly of Applied Mathematics* 10, 157–165.
- Duckworth, W., 1953. Discussion of Ryshkewitch paper by Winston Duckworth. *Journal of the American Ceramic Society* 36, 68. doi:[10.1111/j.1151-2916.1953.tb12838.x](https://doi.org/10.1111/j.1151-2916.1953.tb12838.x).
- Duncan, J.M., Chang, C.Y., 1970. Nonlinear analysis of stress and strain in soils. *ASCE Journal of the Soil Mechanics and Foundations Division* 96, 1629–1653.
- Edmans, B.D., Sinka, I.C., 2019. Fully implicit integration of elastoplastic models with moduli dependent on plastic state variables. *Computers and Structures (Under Review)*.
- Etsion, I., Kligerman, Y., Kadin, Y., 2005. Unloading of an elastic-plastic loaded spherical contact. *International Journal of Solids and Structures* 42, 3716–3729. doi:<https://doi.org/10.1016/j.ijsolstr.2004.12.006>.
- Fleck, N., Kuhn, L., McMeeking, R., 1992. Yielding of metal powder bonded by isolated contacts. *Journal of the Mechanics and Physics of Solids* 40, 1139–1162. doi:[10.1016/0022-5096\(92\)90064-9](https://doi.org/10.1016/0022-5096(92)90064-9).

- Ghaednia, H., Wang, X., Saha, S., Xu, Y., Sharma, A., Jackson, R., 2018. A review of elastic-plastic contact mechanics. *Applied Mechanics Reviews* 69. doi:[10.1115/1.4038187](https://doi.org/10.1115/1.4038187).
- Hertz, H., 1882. Über die Berührung fester elastischer Körper. *Journal für die reine und angewandte Mathematik*, 156–171.
- Hiestand, E., 1997. Mechanical properties of compacts and particles that control tableting success. *Journal of Pharmaceutical Sciences* 86, 985–990. doi:[10.1021/js9701061](https://doi.org/10.1021/js9701061).
- Hiestand, H., Smith, D., 1984. Indices of tableting performance. *Powder Technology* 38, 145–159. doi:[10.1016/0032-5910\(84\)80043-1](https://doi.org/10.1016/0032-5910(84)80043-1).
- Houlsby, G.T., 1981. A study of plasticity theories and their applicability to soils. Ph.D. thesis. University of Cambridge, UK.
- Jackson, R., Green, I., 2005. A finite element study of elasto-plastic hemispherical contact against a rigid flat. *Journal of Tribology* 127, 343–354. doi:[10.1115/1.1866166](https://doi.org/10.1115/1.1866166).
- Johansson, B., Alderborn, G., 1996. Degree of pellet deformation during compaction and its relationship to the tensile strength of tablets formed of microcrystalline cellulose pellets. *International Journal of Pharmaceutics* 132, 207–220. doi:[10.1016/0378-5173\(95\)04373-X](https://doi.org/10.1016/0378-5173(95)04373-X).
- Johansson, B., Wikberg, M., Ek, R., Alderborn, G., 1995. Compression behaviour and compactability of microcrystalline cellulose pellets in relationship to their pore structure and mechanical properties. *International Journal of Pharmaceutics* 117, 57–73. doi:[10.1016/0378-5173\(94\)00295-G](https://doi.org/10.1016/0378-5173(94)00295-G).
- Kogut, L., Etsion, I., 2002. Elastic-plastic contact analysis of a sphere and a rigid flat. *Journal of Applied Mechanics, Transactions ASME* 69, 657–662. doi:[10.1115/1.1490373](https://doi.org/10.1115/1.1490373).
- Li, F., Pan, J., Sinka, C., 2009. Contact laws between solid particles. *Journal of the Mechanics and Physics of Solids* 57, 1194–1208.
- Macias, K.A., Carvajal, M.T., 2012. The influence of granule density on granule strength and resultant contact strength. *Chemical Engineering Science* 72, 205–213. doi:[10.1016/j.ces.2012.01.026](https://doi.org/10.1016/j.ces.2012.01.026).
- Maeda, K., Miura, K., 1999. Relative density dependence of mechanical properties of sands. *Soils and Foundations* 39, 69–79. doi:[10.3208/sandf.39.69](https://doi.org/10.3208/sandf.39.69).
- Markl, D., Strobels, A., Schlossnikl, R., Bøtker, J., Bawuah, P., Ridgway, C., Rantanen, J., Rades, T., Gane, P., Peiponen, K.E., Zeitler, J.A., 2018. Characterisation of pore structures of pharmaceutical tablets: A review. *International Journal of Pharmaceutics* 538, 188 – 214. doi:[10.1016/j.ijpharm.2018.01.017](https://doi.org/10.1016/j.ijpharm.2018.01.017).
- Mohr, O., 1900. Welche Umstände bedingen die Elastizitätsgrenze und den Bruch eines Materiales? *Zeitschrift des Vereins Deutscher Ingenieure* 44, 1524–1530.
- Roscoe, K.H., Schofield, A.N., Wroth, C.P., 1958. On the Yielding of Soils. *Géotechnique* 8, 22–53. doi:[10.1680/geot.1958.8.1.22](https://doi.org/10.1680/geot.1958.8.1.22).
- Russell, A.R., Wood, D.M., 2009. Point load tests and strength measurements for brittle spheres. *International Journal of Rock Mechanics and Mining Sciences* 46, 272–280. doi:<https://doi.org/10.1016/j.ijrmms.2008.04.004>.
- Shang, C., 2012. Modelling Powder Compaction and Breakage of Compacts. Ph.D. thesis. University of Leicester.
- Shang, C., Sinka, I., Pan, J., 2012. Constitutive model calibration for powder compaction using instrumented die testing. *Experimental Mechanics* 52, 903–916. doi:[10.1007/s11340-011-9542-8](https://doi.org/10.1007/s11340-011-9542-8).
- Shankar, S., Mayuram, M., 2008. Effect of strain hardening in elastic-plastic transition behavior in a hemisphere in contact with a rigid flat. *International Journal of Solids and Structures* 45, 3009–3020. doi:[10.1016/j.ijsolstr.2008.01.017](https://doi.org/10.1016/j.ijsolstr.2008.01.017).
- Sinha, T., Bharadwaj, R., Curtis, J.S., Hancock, B.C., Wassgren, C., 2010. Finite element analysis of pharmaceutical tablet compaction using a density dependent material plasticity model. *Powder Technology* 202, 46–54. doi:[10.1016/j.powtec.2010.04.001](https://doi.org/10.1016/j.powtec.2010.04.001).
- Sinka, I., Cocks, A., Tweed, J., 2001. Constitutive data for powder compaction modeling. *Journal of Engineering Materials and Technology, Transactions of the ASME* 123, 176–183. doi:[10.1115/1.1339003](https://doi.org/10.1115/1.1339003).
- Sinka, I., Cunningham, J., Zavaliangos, A., 2003. The effect of wall friction in the compaction of pharmaceutical tablets with curved faces: a validation study of the Drucker-Prager Cap model. *Powder Technology* 133, 33–43. doi:[10.1016/S0032-5910\(03\)00094-9](https://doi.org/10.1016/S0032-5910(03)00094-9).
- Spriggs, R.M., 1961. Expression for effect of porosity on elastic modulus of polycrystalline refractory materials, particularly aluminum oxide. *Journal of the American Ceramic Society* 44, 628–629. doi:[10.1111/j.1151-2916.1961.tb11671.x](https://doi.org/10.1111/j.1151-2916.1961.tb11671.x).
- Szanto, M., Bier, W., Frage, N., Hartmann, S., Yosibash, Z., 2008. Experimental based finite element simulation of cold isostatic pressing of metal powders. *International Journal of Mechanical Sciences* 50, 405–421. doi:[10.1016/j.ijmecsci.2007.10.004](https://doi.org/10.1016/j.ijmecsci.2007.10.004).
- Trasorras, J., Krauss, T., Ferguson, B., 1989. Modeling of powder compaction using the finite element method, in: *Proceedings of the 1989 Powder Metallurgy Conference & Exhibition*, pp. 85–104.
- Tvergaard, V., 1990. Material failure by void growth to coalescence. *Adv. Appl. Mech.* 27.
- Walton, K., 1987. The effective elastic moduli of a random packing of spheres. *Journal of the Mechanics and Physics of Solids* 35, 213–226. doi:[10.1016/0022-5096\(87\)90036-6](https://doi.org/10.1016/0022-5096(87)90036-6).

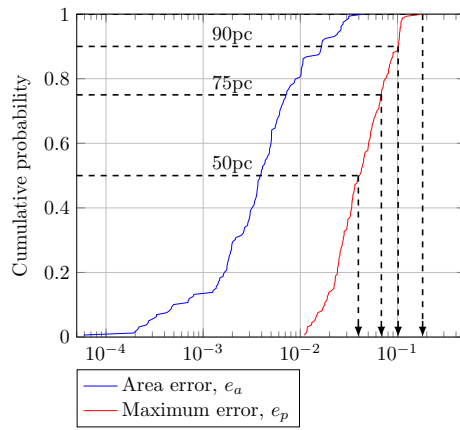
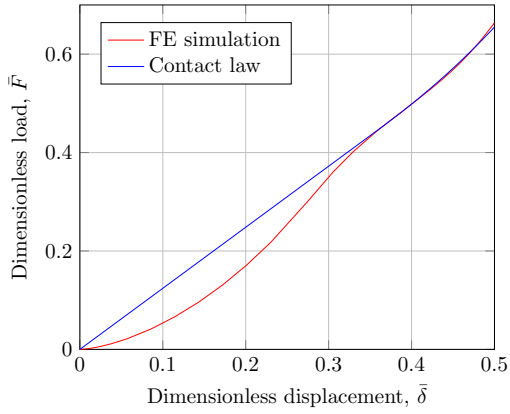
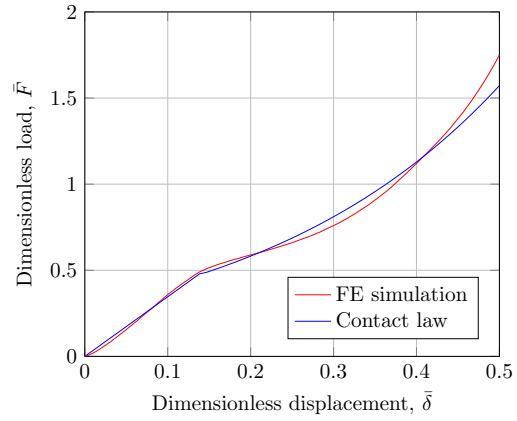


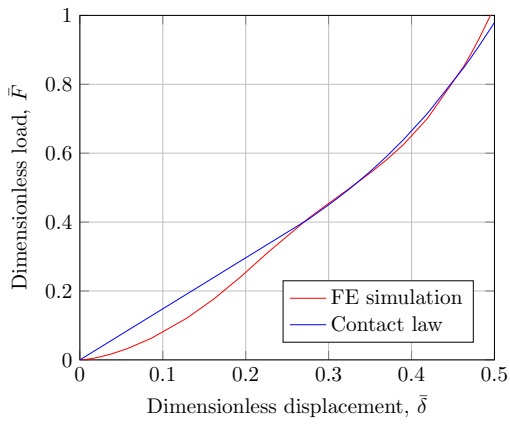
Fig. 11. Distribution of errors in fitting contact law for yield surface shape study, taken over all 160 contact simulations. Error measures are defined by Eqs. 7 and 8, for each load-displacement curve.



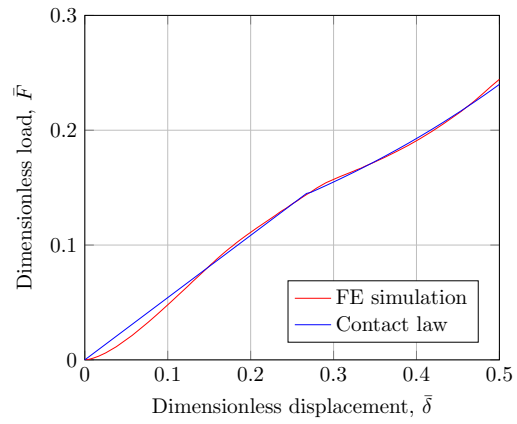
(a) 100th percentile (worst) case for peak error
($\bar{\Gamma}_0=1.0, \bar{\Lambda}_0=0.01, \bar{E}_0=3$)



(b) 90th percentile case for peak error
($\bar{\Gamma}_0=1.0, \bar{\Gamma}_0=0.1, \bar{E}_0=50$)

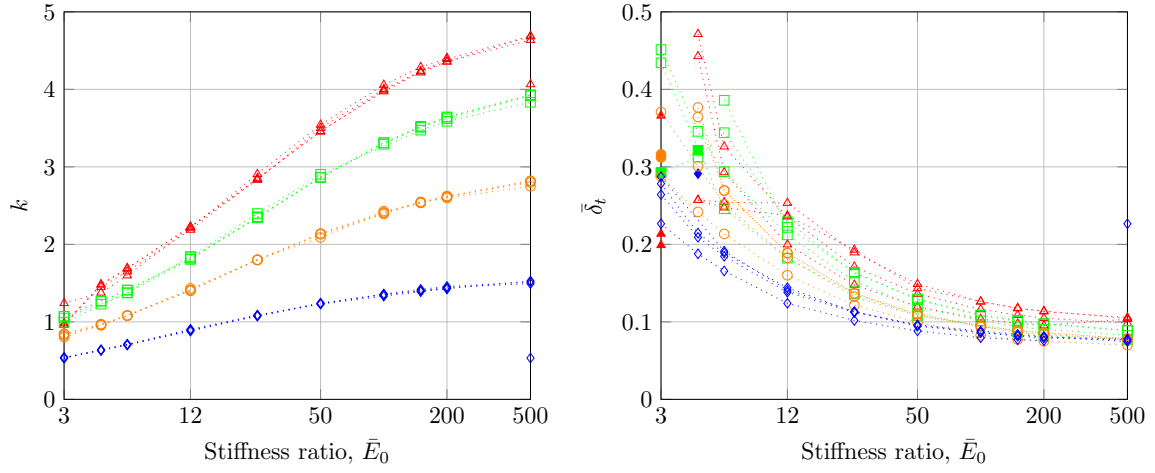


(c) 75th percentile case for peak error
($\bar{\Gamma}_0=1.0, \bar{\Gamma}_0=1.0, \bar{E}_0=4.5$)



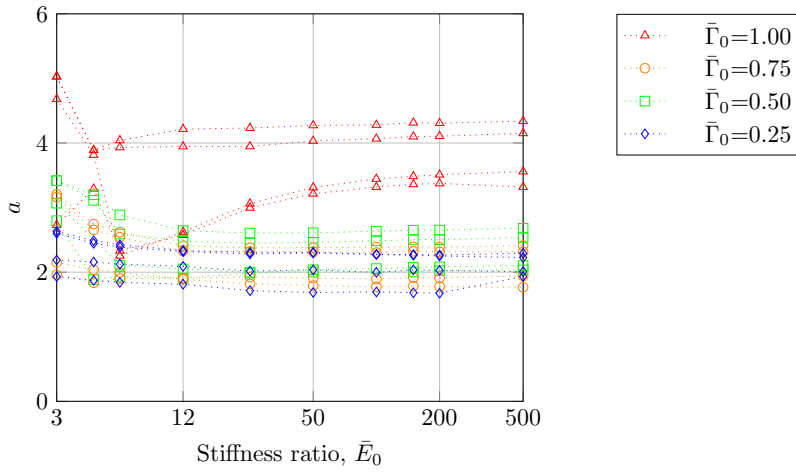
(d) 50th percentile case for peak error
($\bar{\Gamma}_0=0.25, \bar{\Gamma}_0=0.1, \bar{E}_0=3$)

Fig. 12. Example load cases comparing responses from FE models and 3-parameter contact law (a) 100th percentile peak error (largest error), (b) 90th percentile peak error, (c) 75th percentile peak error, (d) 50th percentile peak error (median).



(a) Initial stiffness parameter, k

(b) Transition parameter, $\bar{\delta}_t$



(c) Exponent, a

Fig. 13. Dependence of contact law parameters on general material parameters \bar{E}_0 , $\bar{\Lambda}_0$ and $\bar{\Gamma}_0$, grouped by shear strength ($\bar{\Gamma}_0$). A logarithmic scale has been used on the stiffness axis for all plots.

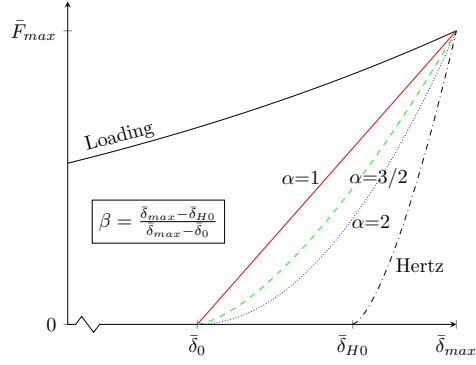


Fig. 14. Sample unloading curves ($\beta < 1$)

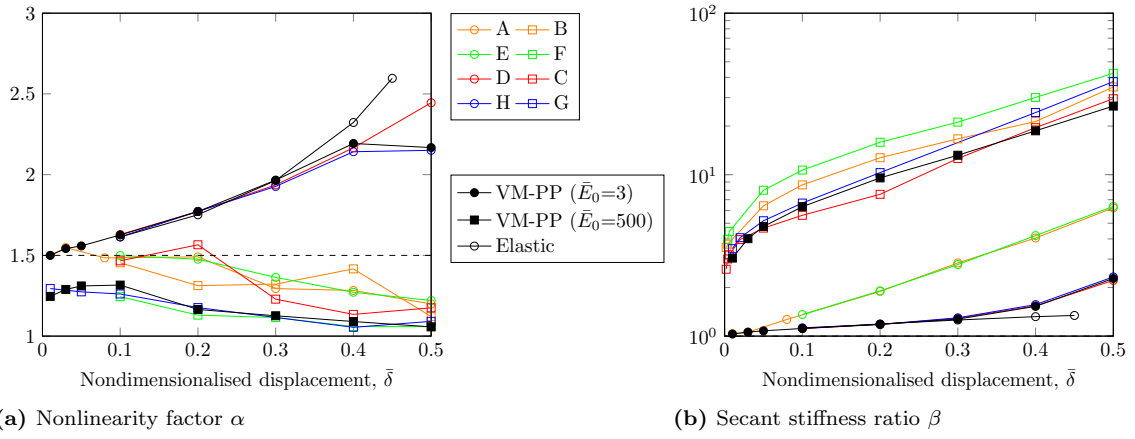


Fig. 15. Unloading law parameters (a) Nonlinearity factor α , (b) Secant stiffness ratio β .

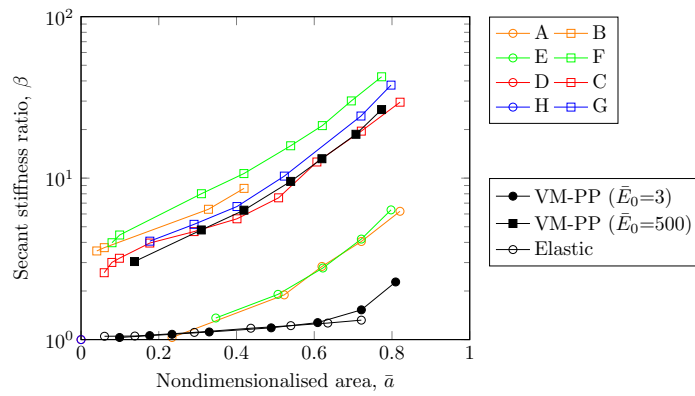


Fig. 16. Variation of secant stiffness ratio with nondimensionalised contact area

614 **Appendix A. Relating contact law parameters to material parameters**

615 The outcome of the parametric study is a model for obtaining the parameters of a contact law (Eq. 6)
 616 from the particle material parameters \bar{E}_0 , $\bar{\Gamma}_0$ and $\bar{\Lambda}_0$, which can be measured experimentally.

Predicting k . Using an augmented bilinear fit for k (Eq. A.1),

$$k(\bar{\Gamma}_0, \bar{E}_0) = a_1 \bar{\Gamma}_0 (\ln \bar{E}_0) + a_2 \bar{\Gamma}_0 + a_3 (\ln \bar{E}_0) + a_4 \quad (\text{A.1})$$

617 gives $a_1 = 7.4613 \times 10^{-4}$, $a_2 = -4.6910 \times 10^{-2}$, $a_3 = 1.8243 \times 10^{-2}$, $a_4 = 0.4262$, with $R^2 = 0.9756$.

618 *Predicting $\bar{\delta}_t$.* Using a biquadratic fit (Eq. A.2) and excluding data with $\bar{E}_0 < 4.5$,

$$\bar{\delta}_t(\bar{\Gamma}_0, \bar{E}_0) = a_1 \bar{\Gamma}_0^2 + a_2 \frac{\bar{\Gamma}_0}{\bar{E}_0} + \frac{a_3}{\bar{E}_0^2} + a_4 \bar{\Gamma}_0 + \frac{a_5}{\bar{E}_0} + a_6 \quad (\text{A.2})$$

619 gives $a_1 = -6.487210 \times 10^{-2}$, $a_2 = 6.271110 \times 10^{-1}$, $a_3 = -1.9770$, $a_4 = 1.1830 \times 10^{-1}$, $a_5 = 9.8478 \times 10^{-1}$,
 620 $a_6 = 4.3846 \times 10^{-1}$, with $R^2 = 0.8725$.

Predicting a . Using a biquadratic (Eq. A.3) fit for a , excluding data with $\bar{E}_0 < 4.5$,

$$a(\bar{\Gamma}_0, \bar{E}_0) = a_1 \bar{\Gamma}_0^2 + a_2 \frac{\bar{\Gamma}_0}{\bar{E}_0} + \frac{a_3}{\bar{E}_0^2} + a_4 \bar{\Gamma}_0 + \frac{a_5}{\bar{E}_0} + a_6 \quad (\text{A.3})$$

621 gives $a_1 = 4.8807$, $a_2 = -3.5557$, $a_3 = 1.5682 \times 10^1$, $a_4 = -3.9942$, $a_5 = -8.9363 \times 10^{-1}$, $a_6 = 2.8104$, with
 622 $R^2 = 0.7115$.

623 Although the general trends for the three parameters can be observed by inspection of Figures 13a,
 624 13b and 13c, and can be explained with reference to mechanisms, the regression results above show there
 625 remains unexplained variation in the results. Particularly at low values of nondimensional stiffness, the
 626 results deviate from the general trends. In particular, two features that require explanation are the fact
 627 that the transition to an exponential load-displacement response is earlier than expected for models with
 628 low nondimensional stiffness (Figure 13b) and the fact that the final stiffening rate for shear-strong particles
 629 is reduced for some values of nondimensional stiffness (Figure 13c). It appears that the persistence of
 630 elastic behaviour into later stages of the particle deformation makes the development of plastic flow zones
 631 more complicated. Low values of nondimensional stiffness seem to result in a nonlinear response in the first
 632 section of the load-displacement response. This can be appreciated by noting the combinations of parameters
 633 which cause the greatest deviations from the linear exponential contact law (Figure 12). Consequently, a
 634 modification to the first part of the contact law in line with solutions obtained for fully elastic spheres
 635 under large displacement, could be considered. The values of the contact law parameters obtained in the
 636 secondary fittings might then be more regular. The predictive relations listed in this Appendix could be
 637 improved with the addition of more polynomial terms of the introduction of transcendental terms. These
 638 ideas have not been pursued in the current work because (1) the three-term linear/exponential contact law
 639 is simple and provides a good fit for the majority of the load-displacement responses and (2) additional
 640 mechanisms in the particle deformation that could be linked to additional terms in the secondary fitting
 641 to give them physical meaning have not yet been identified. It is noted that the internal evolution of the
 642 particle has been mapped for the eight extreme cases only (Figure 10), where already it is evident that
 643 there is no universal deformation scheme that can be related to individual cases by a mapping dependent
 644 on the material parameters, as has been attempted for the VM-PP model; additional evolution patterns for
 645 intermediate combination should be revealed by further investigation.